Multi-tier mechanics control stromal adaptations in swelling lymph nodes

Frank P. Assen[1,2,*], Miroslav Hons[1,3], Robert Hauschild[1], Shayan Shamipour[1], Jun Abe[4], Walter A. Kaufmann[1], Tommaso Costanzo[1], Gabriel Krens[1], Markus Brown[1], Burkhard Ludewig[5], Simon Hippenmeyer[1], Jens V. Stein[4], Carl-Philipp Heisenberg[1], Edouard Hannezo[1], Sanjiv A. Luther[6], Michael Sixt[1,*]

[1]Institute of Science and Technology Austria (IST Austria), Klosterneuburg, Austria

[2]Department of Dermatology, Medical University Vienna, Vienna, Austria

[3]BIOCEV, First Faculty of Medicine, Charles University, Vestec, Czech Republic

[4]Department of Oncology, Microbiology and Immunology, University of Fribourg, Fribourg, Switzerland

[5]Institute of Immunobiology, Kantonsspital St Gallen, St Gallen, Switzerland

[6]Department of Biochemistry, University of Lausanne, Epalinges, Switzerland

[*]Correspondence to: Sixt@ist.ac.at; frank.assen@meduniwien.ac.at

Abstract

Lymph nodes (LNs) comprise two main structural elements: Fibroblastic reticular cells (FRCs) that form dedicated niches for immune cell interaction and capsular fibroblasts that build a shell around the organ. While LNs are fairly stable in size during homeostatic conditions, immunological challenge causes more than 10-fold increase in size within only a few days. How a solid organ can accommodate such extreme volumetric changes is poorly understood. Here, we characterize the biomechanics of LN swelling on the cellular and organ scale. We identify lymphocyte trapping by influx and proliferation as drivers of an outward pressure force, causing FRCs and their associated conduits to stretch. After an initial phase of relaxation, FRCs sense the resulting strain via cell matrix adhesions, which coordinates local growth and remodeling of the stromal network. While the expanded FRC network adopts its typical configuration, a massive fibrotic reaction of the organ capsule sets in and counters further organ expansion. Thus, different fibroblast populations mechanically control LN swelling in a multi-tier fashion.

Introduction

Lymph nodes (LNs) are the macroscopic organs of the adaptive immune system. As opposed to other organs, the LN parenchyma only contains few resident cells, while the bulk of lymphocytes is in transit. Lymphocytes circulate through the bodies' vascular systems, and from there they enter LNs via high endothelial venules (HEVs). Within the LN parenchyma, lymphocytes actively migrate to scan large numbers of potentially antigen-bearing dendritic cells (DCs). After several hours of unsuccessful search, lymphocytes exit the organ again via efferent lymphatic vessels that eventually drain back into the blood circulation and the cycle starts again[1,2]. Lymphocytes are densely packed within LNs and make up about 95% of its total cellularity. Despite dynamic cellular exchange, homeostatic LN size remains relatively stable. Known modulators of homeostatic LN cellularity (e.g., during circadian rhythms[3,4]) are mainly chemoattractants and adhesion molecules[2,5–8], which serve as entry and exit signals for lymphocytes, as well as stromal cell-derived survival factors[9–12] and adrenergic signals[13,14]. The main stromal cells found in LNs are FRCs. These form the non-hematopoietic backbone of the organ and deposit bundled fibers of extracellular matrix (ECM) that assemble an intricate 3D network termed conduits. FRCs enwrap these ECM conduits and form an interface with the immune cells[15,16]. They provide a multitude of signals that serve to compartmentalize the organ and support migration, cellular interactions and expansion of immune cell subsets[17–19].

Upon immunological challenge, reactive LNs swell rapidly by recruiting large numbers of naïve lymphocytes via HEVs, while lymphocyte egress via efferent lymphatics is initially blocked[20,21]. LNs can swell up to 10-fold in size in the order of days, imposing an internal structural problem on the FRC network that has to cope with this volumetric challenge. It has been demonstrated that FRCs are able to relax and expand upon interaction with activated DCs[22,23]. This has been proposed as one mechanism that allows the LN to create additional space during the swelling phase. In addition, FRC numbers expand during inflammation and various redundant mechanisms that drive this expansion in the early and late phase of LN swelling have been described[20,22–26]. The ratio of FRC- to lymphocyte numbers remains fairly constant in the swelling LN and trapping of naïve lymphocytes in the absence of inflammatory stimuli has been demonstrated as a sufficient stimulus for the FRC network to expand[20]. How network expansion is coordinated to prevent under- or

overgrowth of the FRC network is unknown, and although mechanical forces are obvious feedback parameters, these aspects of LN swelling have not been measured until to date. We measure the cellular and mechanical changes accompanying LN swelling and show that mechanical load on the conduit network and subsequent FRC mechanosensing are central to expansion of the FRC network and LN growth.

Results

The reactive lymph node resists swelling

To understand the global mechanical behavior of LNs while expanding, we started out with a quantitative characterization of bulk tissue properties of the reactive organ. Upon immunization with keyhole limpet hemocyanin in complete Freund's adjuvant (KLH/CFA) in footpads of wild-type (wt) mice, we observed a more than 10-fold increase in volume of draining popliteal LNs after 14 days, when the organ reached its maximum size. The volume was calculated from 2D side-view images, which correlated well with the weight of the organ and showed that LNs swell on average about 0.75 mm^3 per day (Figure 1A,B & Figure S1A,B). We measured tissue mechanics by compressing explanted popliteal LNs between two parallel plates at 75% of their original height (25% strain), while the resisting force exerted by the LN on the top plate was measured over a time period of 20-60 minutes (Figure 1C). During this time the LN underwent a viscoelastic relaxation behavior and reached a new force-equilibrium, which is described by the stress-relaxation curve (Figure 1D & Figure S1C,D). Together with the geometrical parameters of LNs measured before compression and at the new force-equilibrium, the *effective resistance* (σ, *surface tension*), the *viscosity* (μ_2, fluidic resistance to deformation by an applied force), and the *elastic modulus* (Young's Modulus, or elastic resistance to deformation by an applied force) of the tissue were derived by modelling the parameters to a generalized Kelvin model (Figure S1E)[27]. At equilibrium (long time scale), the LN resisted the external force exerted by the plate, which sets the *effective resistance* (given in Newton/m). This parameter describes the collective forces resisting organ expansion and is a measure of how much force is necessary to drive the swelling of the LN by a certain length scale.

During the course of organ expansion (D0-D14), we observed a ~4-fold increase of effective resistance and values remained elevated until the endpoint at D14 (Figure 1E). Viscosity – the resistance to deformation on the medium time scale – only increased in the last phase of swelling, while elasticity – the resistance to deformation on the short time scale – was selectively increased from the homeostatic condition at D2 and D14 of inflammation (Figure 1F,G).

These data demonstrate that tissue properties of LNs show complex adaptive dynamics upon swelling, and suggest that the mechanical features of the organ resist the forces driving expansion.

Lymphocyte numbers generate pressure and drive lymph node swelling

Having defined that mechanical properties of the LN resist swelling, we next asked what are the internal forces driving organ expansion. Lymphocytes constantly recirculate through LNs where they are densely packed within the FRC scaffold (Figure S1F). Entry via HEVs, blocking of exit in the early inflammation phase, and proliferation upon activation are the main factors that increase cellularity of the node, making these potential factors driving expansion[28–30]. Hence, we manipulated entry and activation and tested the impact on LN bulk tissue properties.

We first perturbed lymphocyte entry under homeostatic conditions using an L-selecting antagonizing antibody; anti-CD62L (α-CD62L). L-selectin is expressed on naïve lymphocytes and rate-limiting for transmigration via HEVs[31]. After 24h of either α-CD62L or PBS intravenous (i.v.) injection, popliteal LNs from wt mice were harvested and used for parallel plate compression experiments. We found that blocking of lymphocyte entry significantly reduced LN volume, effective resistance and viscosity, while the Young's Modulus remained unchanged (Figure 2A-E). These data suggest that lymphocyte influx represents an internal force, balancing the effective resistance of the homeostatic LN.

Next, we asked how lymphocyte cellularity affects bulk tissue properties of LNs during inflammatory swelling. In order to distinguish between contribution of recirculating and locally proliferating lymphocytes, we treated wt or OT-II mice with either α-CD62L or PBS, immunized with KLH/CFA and measured tissue properties after four days (Figure 2F-J). Mice carrying the OT-II TCR transgene suppress their natural TCRs [31], thereby creating a situation where lymphocyte homing is maintained but the majority of B and T cell responses against the mismatched KLH antigen eliminated. Homing, and to a lesser extent proliferation, contributed significantly to LN swelling, while elimination of both parameters reduced LN volumes even further (Figure 2G). In agreement with the findings under homeostatic conditions, α-CD62L administration reduced the effective resistance in both wt and OT-II mice, with blockade of homing showing the dominant effect (Figure 2H). While the viscosity in the tested conditions did not show a clear trend with lymphocyte cellularity, the Young's

Modulus was reduced when lymphocyte trafficking was blocked in inflammation (Figure 2I,J).

Thus, lymphocyte trapping is not a consequence of LN swelling but drives the process as it generates an outward pressure force which is countered by the organ's effective resistance.

The FRC network stretches upon lymph node swelling

Next, we investigated which mechanical features of the LN are resisting it's expansion. The two candidate structures mediating the LNs effective resistance to swelling are the organ capsule, and the FRC- and conduit network. To understand how the FRC network adapts to volumetric changes upon swelling we quantified FRC spacing (gaps) within the T zone over the time course of inflammation in Ccl19-Cre; mTmG (FRC-mGFP) (membrane Tomato, membrane Green Fluorescent Protein (GFP)) mice that selectively express membrane GFP (mGFP) in FRCs[32,33]. To this end, a circle-fitting algorithm was used to quantify the distribution of gaps in FRC networks from two-dimensional (2D) tissue sections (Figure 3A,B). While we found no obvious disruptions of network integrity, the FRC network dynamically adapted over time. In the first four days of inflammation the FRC network widened, as indicated by larger gaps, and in the following days returned to homeostatic levels (Figure 3C,D).

These results suggest that the intact FRC network initially stretches upon swelling and subsequently remodels to accommodate the increased numbers of proliferating and immigrating lymphocytes.

Conduits are stretched in the swelling lymph node

The FRC network comprises two principal structural components: the FRC itself and the ECM conduit, a complex fibrillar structure, which the myofibroblastic FRC both produces and ensheathes (Figure 4A). Both components have the potential to bear load and confer mechanical resistance to swelling. In the following, we devised strategies to quantitatively measure if and to what extent the two structures experience mechanical forces. We started out with the ECM component and as a proxy for mechanical strain, we chose to investigate the structural organization of the conduit's fibrillar collagen. Like in tendons and other elastic ECM structures, fibrillar alignment should increase with strain.

161 We fixed homeostatic and reactive LNs and removed all cellular components by alkali-
162 maceration (Figure S2A,B). To resolve the 3-dimensional (3D) organization of individual
163 collagen fibrils, scanning transmission electron microscopy (STEM) tomograms of T zone
164 conduits were acquired at 2 degrees differential tilting angles (Figure 4A). 3D images were
165 reconstructed using computed weight back projection (Figure S2C,D). We quantified the
166 extent of conduit stretching by 3D manual tracking of individual collagen fibril segments and
167 by computationally calculating the centerline of each conduit based on the average
168 direction of its collagen fibrils. This allowed us to determine the angle of misalignment of
169 individual fibril segments relative to the centerline (Figure 4C,D). We found that compared
170 to homeostasis (D0), early in inflammation (D2, D4) conduit collagen fibrils become
171 progressively aligned, whereas later in inflammation (D14) they again adopted a misaligned
172 configuration (Figure 4D).
173 These results suggest that conduits stretch and bear an increased mechanical load early
174 upon LN swelling. At later time points they revert to the homeostatic state. Initial stretching
175 and later adaptation are well in line with our previous findings on network configuration.
176
177 **FRC network tension increases upon lymph node swelling**
178 We next addressed the cellular component of the FRC stretching-response. To study if the
179 previously observed change in conduit conformation is mirrored by the tension-state of the
180 FRC network, we directly measured FRC network tension by intravital laser ablation and
181 recoil analysis[34,35]. To this end, inguinal LNs of FRC-mGFP mice were surgically exposed and
182 the FRC network was imaged around 20 µm below the capsule. Individual strands of the 3D
183 network were cut using a high-power ultra-violet (UV)-laser (Figure 5A). FRC network
184 tension was subsequently determined in kymographs by calculating local recoil velocities of
185 the region around the site of ablation (Figure 5B,C and Supplemental Movie 1). We found
186 that at D4 and D8 of inflammation the tension on the FRC network almost doubled and was
187 restored again to homeostatic levels at D14 of inflammation.
188 As a proxy for the cellular mechano-response, we next measured the nuclear vs. cytoplasmic
189 intensity of the transcription factors Yes-associated protein (YAP), and transcriptional co-
190 activator with PDZ binding motif (TAZ), which are well-established downstream responses of
191 cytoskeletal tension[36]. FRCs and endothelial cells stained positive for YAP/TAZ, while no
192 signal could be observed in leukocytes (Figure 5D,E). The nuclear:cytoplasmic ratio of

YAP/TAZ (N:C YAP/TAZ ratio) in FRCs remained stable from D0 to D2 of inflammation but increased at D4 and D8 of inflammation, confirming that FRCs experience increased cytoskeletal tension during LN swelling. The N:C ratio decreased after FRC tension peaked (Figure 5C,F), thereby faithfully recapitulating the tension as measured by laser cutting. Interestingly, after two weeks of inflammation we observed a large population of FRCs that had a negative N:C ratio, suggesting that those cells were completely shielded from active tension.

Together, these data demonstrate that FRC tension increases upon LN swelling. However, compared with the ECM conduit (Figure 4), tension at the cellular level increases with a two day time delay. This kinetic is well in line with previous observations, suggesting that early in inflammation FRCs experience a relaxation of actomyosin contractility[22,23]. This relaxation is transient and followed by an increase in cytoskeletal tension. At later time points when network geometry adopts its homeostatic configuration, tension drops again.

FRCs in the swelling lymph node undergo distributed clonal expansion

The above data suggest that lymphocyte influx drives LN expansion, which initially stretches the FRC network and elicits a mechanosensitive response by the cells, once their initial relaxation[22,23] ceases. We next wanted to understand how the FRC network expands, remodels and re-establishes its typical configuration and mechanical state, while maintaining structural integrity.

To this end, we devised an approach to map the spatio-temporal expansion of the FRC network in the swelling LN *in situ*. We used a sparse clonal labeling approach named Mosaic Analysis with Double Markers (MADM)[37–39]. MADM labeling depends on rare interchromosomal mitotic recombination driven by Cre-loxP sites (Figure S3A,B). Two reciprocally split GFP and tdTomato genes (GT and TG) on identical loci of homologous chromosomes are used to create transheterozygous offspring (GT/TG). Interchromosomal recombination can take place in G_2 phase and restores functional GFP and tdTomato expression. To trigger rare recombination specifically in FRCs we used the Ccl19-*Cre* transgene[32]. When followed by X-segregation of chromosomes in mitosis, two daughter cells are formed in which one expresses GFP (green lineage) and the other tdTomato (red lineage). Recombination is irreversible and all subsequent progeny cells become part of the lineage.

225 Homeostatic and reactive LNs were cleared and imaged by 3D light-sheet fluorescence
226 microscopy (LSFM). In reactive nodes, prominent clusters of FRCs emerged at D4 and D8 of
227 inflammation, while such clusters were rarely observed in homeostasis (Figure 6A,B & Figure
228 S3C). This suggested that individual FRC clones expanded following immunization and that
229 daughter-FRCs stay close to their precursor. No substantial bias in red vs. green lineage was
230 apparent, justifying combined analyses (Figure S3D). FRC clusters were quantitatively
231 analyzed using a density-based spatial clustering of applications with noise (DBSCAN)[40] for
232 which FRC bodies were semi-automatically mapped in 3D as spheres with a 12 µm diameter
233 (Figure S3E). A cluster was defined as at least three FRCs from the same lineage within a
234 radius of 20 µm. We found that both the number of labeled FRCs, number of clusters and
235 number of FRCs in clusters were significantly increased in reactive nodes (Figure 6C-F). Since
236 clusters can arise by chance, the cluster results were compared to the average of 10
237 simulated distributions in which the same number of FRCs were randomly distributed in the
238 same volume. Although clusters arise by chance in random distributions, FRCs in
239 inflammation were less uniformly distributed and formed more and larger clusters with FRC
240 numbers ranging from 3-14 (Figure 6G, Figure S3F). Clone size distribution was exponential
241 as is expected from an equipotent population of precursors that are dividing
242 stochastically[41]. To quantify the extent of FRC clustering within LNs, we defined a cluster
243 factor (CF) as the ratio of the number of FRCs found in clusters between the observed and
244 simulated distributions (Figure S3G). Hence, a CF of 100 indicates that 100x more cells are
245 found in clusters as by chance alone. We found an average CF of 5 in homeostatic conditions
246 and 117 in inflammation (respectively, 70 and 165 for D4 and D8), confirming that FRCs
247 form clusters in the swelling LN (Figure 6H).
248 We next investigated if FRC clusters are found at the vicinity of HEVs in the swelling LN as it
249 has been shown that *de novo* FRCs can derive from perivascular fibroblasts in the
250 developing spleen[42,43]. To this end, the CF was plotted as a function of the distance from
251 HEVs. No enrichment of clusters was found at these specific perivascular areas (Figure 6I).
252 To better understand the relationships between the measured parameters a correlation-
253 matrix was created (Figure 6J). As expected, the number of labeled FRCs correlated with the
254 number of observed clusters and the number of FRCs found in clusters, while the number of
255 clusters correlated well with the number of FRCs found in clusters. In the reactive LN *de*
256 *novo* MADM-events can occur, but our data indicate that these do not affect the CF as the

257 CF is independent of the number of labeled FRCs, and the relative numbers of FRC in
258 clusters remains unchanged in inflammation (Figure 6J, Figure S3H). LN volume was the best
259 determinant for the CF and also correlated well with the number of labeled FRCs, number of
260 clusters and FRCs in clusters (Figure 6J,K).
261 Together, these data show that FRCs expand in randomly distributed clusters and that FRC
262 growth correlates with LN volume (Figure 6K). This suggests that FRCs can expand in
263 response to local signals independent of their localization.
264
265 **Talin1 is required for FRC mechanosensing.**
266 Given our previous observations, mechanical forces appeared as an attractive feedback
267 parameter regulating FRC network growth. Mechano-coupling of fibroblasts to their
268 underlying matrix is mediated by integrins and their associated intracellular force-sensitive
269 adaptor molecule talin. FRCs express both Talin1 and Talin2 isoforms which play non-
270 redundant roles in integrin activation and force transduction[44]. We selectively deleted
271 Talin1 in FRCs by generating Ccl19-*Cre; Talin1fl* ($FRC^{\Delta TLN1}$) mice.
272 Peripheral LNs of $FRC^{\Delta TLN1}$ mice were reduced in size and had lowered levels of the T-zone
273 chemokine CCL21 in the paracortex and the T cell zone was significantly reduced in size in
274 $FRC^{\Delta TLN1}$ LNs (FigureS4A-C). Within the T cell zone podoplanin (PDPN)+ $FRCs^{\Delta TLN1}$ still formed
275 a regularly interconnected network and expressed intercellular adhesion molecule 1 (ICAM-
276 1) and vascular cell adhesion molecule 1 (VCAM-1), arguing for regular differentiation
277 (Figure S4D). Within HEVs, CCL21 levels were unaffected (Figure S4B). Hence, despite the
278 reduced size, the basic organization and differentiation of the Talin1 deficient FRC network
279 was maintained. When $FRC^{\Delta TLN1}$ mice were immunized with KLH, LN swelling was substantial
280 (Figure7A) and during the initial four days after immunization, relative weight gain was
281 comparable to control mice. A mild reduction was only seen at D14. This demonstrates that
282 lymphocyte influx and proliferation were still occurring within the Talin deficient FRC
283 network, emphasizing the suitability of the genetic model to ask the principal question, if
284 FRC mechanosensing is required for network adaptation.
285 When we analyzed N:C YAP/TAZ ratio almost no $FRCs^{\Delta TLN1}$ showed a nuclear localization
286 both under homeostatic and reactive conditions (Figure 7B,C). This finding demonstrates
287 that Talin1 dependent mechanotransduction in FRCs is rate-limiting for YAP/TAZ nuclear
288 translocation and strongly indicate that $FRCs^{\Delta TLN1}$ lose their mechanosensitivity. To assess

289 the functional consequences for FRC network integrity we performed *in situ* network
290 analysis. To this end, 3D volumes of FRC networks were acquired from cleared thick
291 vibratome slices and network spacing was quantified using a 3D sphere-filling algorithm
292 (Figure 7D,E). In agreement with the previous 2D GAP analysis (Figure 2) the network of
293 control mice widened and remained intact at D4 of inflammation. The FRC$^{\Delta TLN1}$ network
294 under homeostatic conditions was widened compared to controls, but structurally intact.
295 Upon immunization the FRC$^{\Delta TLN1}$ network integrity became severely compromised, showing
296 large FRC-free gaps (Figure 7D,E & S4E). These defects were most apparent at D4 and partly
297 recovered by D14 of inflammation.
298 These data suggest that the FRC network in FRC$^{\Delta TLN1}$ mice failed to adapt to organ swelling
299 and partly disintegrated or ruptured. To investigate the fate of FRCs under these conditions
300 thick vibratome sections were stained for cleaved caspase 3 (cC3) and Ki67, to identify
301 apoptotic and proliferating FRCs, respectively (Figure 7F,G). These analyses showed little
302 apoptotic and proliferating FRCs in FRC$^{\Delta TLN1}$ and control mice under homeostatic conditions.
303 At D4 after immunization, the number of apoptotic FRCs per volume increased significantly
304 in FRC$^{\Delta TLN1}$ mice as compared to controls, while proliferation was similar in both control and
305 knockout. At D8, apoptotic FRCs per volume unit were still larger in FRC$^{\Delta TLN1}$ compared to
306 controls and proliferating FRCs were increased (Figure 7F,G).
307 These data indicate that compromised mechanosensing causes a severe dysregulation in
308 survival and proliferation of the FRC compartment, which leads to a loss of network
309 integrity. This finding is line with the idea that FRC remodeling is locally controlled by
310 mechanical feedback.
311
312 **Capsule fibrosis constrains lymph nodes at late time points**
313 Network analysis and tension measurements indicated that the FRC network reached a
314 "new equilibrium" two weeks after immunization, because it adopted its homeostatic
315 configuration. Nevertheless, effective resistance remained high at these late time points,
316 raising the question if another structure contributes to the force balance.
317 The LN capsule can be divided into two components: a floor that includes floor lymphatic
318 endothelial cells (fLECs) along with a basement membrane that connects to conduits, and a
319 roof that consists of ECM with embedded lymphoid fibroblasts to which ceiling lymphatic

endothelial cells (cLECs) adhere. We investigated the structural and mechanical properties of the two capsule components in homeostatic and inflammatory conditions.

fLECs are sparsely labeled in FRC-mTmG mice, as is demonstrated by their double positivity for mGFP and LYVE-1, and their location in the floor of the subcapsular sinus (SCS) (Figure S5A). Since the SCS floor is densely populated by fLECs, we used this sparse labeling to our advantage as it enabled the measurement of active tension on single fLECs *in vivo* using UV-laser ablation (Figure 8A). We found that fLECs had high levels of basal tension that exceeded those of FRCs (Figure 8B). Interestingly, after two days of inflammation fLECs showed reduced tension that was reverted to homeostatic levels in the further swelling phase. Likewise, no rise in active tension on the long time scale (D8-D14) was found on the capsule ECM following UV laser ablation of explanted popliteal LNs (Figure S5B,C).

The absence of a continuous rise in active tension on the capsule floor and roof entails that these components are being remodeled to keep up with the volumetric increase of the swelling LN. The capsule was therefore assessed by histology in Prospero homeobox protein 1 (Prox1)- GFP mice in which the cytoplasm of all LECs is labeled with GFP. Additional 4,6-diamidino-2-phenylindole (DAPI) and platelet-derived growth factor receptor- β (PDGFR-β) staining allowed the measurement of capsule thickness and mesenchymal cell layers of the capsule above the SCS in homeostasis and inflammation. We found that the capsule thickness remained unchanged in the first four days of inflammation. Strikingly, the capsule thickness increased ~14-fold from D8 to D14 of inflammation, forming a dense fibrotic layer between the parenchyma and surrounding adipose and muscle tissue, while the SCS remained intact (Figure 8C,D & Figure S5D).

We asked if such significant remodeling of the capsule resulted in changes in its mechanical properties. To this end a micro-pipette with a small diameter was used to locally aspirate ERTR7 labeled capsules of popliteal LN explants. Using Laplace's law, an effective Young's modulus of the capsule was derived (Figure 8E). We found that the elastic modulus of the capsule remained stable over the first eight days of inflammation but was doubled at D14 (Figure 8F). By multiplying the capsule thickness and Young's modulus of the capsule, we derived the passive capsule tension; a measure of the amount of force necessary to enlarge the whole thickness of the capsule by a certain length, i.e. the force needed to swell the LN. The passive tension showed a substantive increase from D0 to D8 of inflammation and kept rising to a massive 150-fold increase at D14 of inflammation (Figure 8G).

These data indicate that during a sustained immune response, tension dissipates from the remodeling FRC network at the intermediary time scale (D4-D14), while the capsule remodels and becomes thicker, stiffer and more resistant to swelling at the long time scale (D8-D14), establishing a new force-equilibrium within the organ that resists further swelling (Figure 8H).

358 **Discussion**

359 Like glia cells of the nervous system, lymphatic stroma cells were long considered the
360 passive structural elements of the immune system. Only the last two decades revealed that
361 the stromal compartment decisively orchestrates immune cell encounters by providing
362 trophic and tactic cues and that in turn stromal cells dynamically respond to signals
363 provided by the immune cells[18,19]. Despite palpation of reactive LNs being part of every
364 physical exam and LNs being unmatched in their ability to change volume, the mechanical
365 aspects of LN swelling have never been directly addressed. By measuring organ mechanics
366 across different time and size scales we establish that reactive swelling of the LN is a multi-
367 tier process controlled by mechanical feedback. This allows the organ to expand in a step-
368 wise controlled fashion, without compromising its delicate architecture.

369 We demonstrate that upon inflammation, accumulating lymphocytes inflate the node and
370 initially stretch the FRC network. This is in line with previous findings that FRCs show an
371 early and transient increase in cell size[20]. Stretching puts tension on the ECM conduit as
372 revealed by a straightened configuration of its ECM fibrils. Although our ultrastructural
373 analysis did not show obvious ruptures of fibrillar collagen, Martinez et al.[45] detected gaps
374 in the ECM (but not the cellular) compartment of swelling LNs, raising the possibility that in
375 some areas of the LN, flexibility of the ECM cannot keep up with cellular deformation.
376 Interestingly, both our laser cutting experiments and the kinetics of nuclear shuttling of
377 YAP/TAZ revealed that compared to their ECM conduit, FRCs experience cytoskeletal
378 tension only with a time delay of two days. This is well in line with findings of the labs of
379 Turley and Reis e Sousa, who showed that early LN swelling is accompanied by a relaxation
380 of the FRC system, allowing the network to stretch[22,23]. Mechanistically, they demonstrated
381 that CLEC-2 ligand expressed on activated DCs binds podoplanin on FRCs and that this
382 interaction relaxes actomyosin contractility within the FRC myofibroblastic network. Such a
383 transient FRC relaxation explains why tension-increase of the ECM conduit precedes
384 tension-increase of FRCs and implies that the FRC cytoskeleton only experiences significant
385 tension once the DC-mediated relaxation signals fade after three to four days. Accordingly,
386 FRCs show increased αSMA expression only after the initial days of inflammation[20].

387 While the FRC network uses its intrinsic pliability to accommodate short-term volumetric
388 changes, sustained strain on the FRC cytoskeleton triggers the next stage of LN swelling,
389 which is characterized by actual growth and structural remodeling of the network. Our

results on genetic ablation of Talin1 in FRCs strongly support the idea that adhesion-dependent mechanosensing is a critical feedback parameter that locally controls growth and survival of the network, so that it reverts to its typical geometry, while being increased in size. In line with these results, mice with a gain of function mutation in the mechanosensitive YAP/TAZ pathway show fibrotic LNs with impaired FRC differentiation[46] and blockade of β1 integrin triggered FRC apoptosis in swelling (but not in homeostatic) LNs[47]. A critical prerequisite of a model where FRC mechanosensing locally controls network remodeling is that the FRC responsiveness is not restricted to specific niches but rather distributed throughout the organ. Our clonal analyses show that this is indeed the case and match results in follicular dendritic cells and marginal reticular cells that were also shown to undergo clonal expansion[48].

Beyond a week of structural adaptation the FRC network of the now massively enlarged LN seemed to reach a new "mechanical equilibrium" as indicated by gap analysis, ECM alignment, tension measurements and YAP/TAZ translocation. Nevertheless, bulk mechanical properties of the LN did not return to homeostatic levels. They rather showed an elevated effective resistance, indicating that another structure now countered the internal pressure generated by the trapped lymphocytes. We thus turned to the capsule as the second major stromal element and found that during these late stages, thickness and mechanical strength of the capsule were massively increased, explaining resistance to further organ expansion. Although capsule fibrosis is a characteristic histopathological descriptor of reactive LNs[49], its mechanistic contributions are completely unexplored and future studies will hopefully show how it contributes to sustained or chronic immune responses.

As the multi-tier model of LN swelling moves through a succession of check-points, it has the advantage of being adaptable to very different types of swelling-scenarios. Transient swelling, as it occurs e.g. during circadian fluctuations, might stretch the network, but is unlikely to cause structural remodeling. In contrary, sustained immune responses with massive lymphocyte trapping and germinal center reactions, might rely on a fibrotic strengthening of the capsule in order to limit excessive expansion of the organ.

420 ## Methods

421

422 **Animals**

423 All animal experiments are in accordance with the Austrian law for animal experiments.
424 Permission was granted by the Austrian Federal Ministry of Science, Research and Economy
425 (identification code: BMWFW 66.018/0010-WF/V/3b/2016). Mice were bred and
426 maintained at the local animal facility in accordance IST Austria Ethical Committee or
427 purchased from Charles River and maintained at the local animal facility in accordance with
428 IST Austria Ethical Committee. OT-II (Stock No: 004194) was bought from JAX. Ccl19-Cre
429 mice have been described previously[32]. MADM-7[39] and Talin1floxed[50] mice were provided
430 by Simon Hippenmeyer and David Critchley, respectively. All mice are on a C57BL/6J
431 background, with exception of MADM-7 which have a CD-1 background. Mice of both sexes
432 between the age of 6 to 20 weeks were used for experiments. For immunization, KLH
433 protein was dissolved in PBS to 5 mg/mL of and then mixed 1:1 with CFA (both Sigma-
434 Aldrich) upon which 40 µL of the immunization mixture was injected in footpads and flanks
435 of draining popliteal and inguinal LNS. LNs were harvested after various timepoint up to
436 two weeks of induction of immunization to be used for histology or explant experiments, or
437 used for *in vivo* imaging experiments. For LN cellularity manipulation experiments, mice
438 were i.v. injected with 100 µg α-CD62L (MEL14) (BioXCell), and control mice with PBS alone.
439 For steady-state evaluation, LNs were harvested 24h after injections were given, and for
440 inflammation conditions injections were given at onset of inflammation. Mice were
441 anesthetized by isoflurane inhalation (IsoFlo, Abbott) for all injection-based experiments, or
442 anaesthetized with a ketamine/xylazine/acepromazine mixture for *in vivo* imaging
443 experiments.

444

445 **Histology and Imaging**

446 LNs were fixed in 4% paraformaldehyde (Electron Microscopy Sciences) in PB (0.1 M, pH 7.4)
447 at 4°C overnight. For cryosections, tissues were additionally embedded for 24h in a solution
448 of 30% glucose in PB (0.1 M, pH 7.4) before embedding and freezing in Tissue-Tek optimum
449 cutting temperature (OCT) compound (Sakura). Cryostat section (10-12 µm) were collected
450 on Superfrost/Plus glass slides (Thermo Fisher Scientific). Alternatively fixed tissues were

451 embedded in 4% low melting temperature agarose (Invitrogen) after fixation and 100-400
452 µm sections were cut using a vibratome (VT1200S, Leica Microsystems).
453
454 Cryostat sections were air-dried for 2h at room temperature (RT) and washed in PBS.
455 Sections were blocked in SEABLOCK blocking buffer (Thermo Fisher Scientific) or in 5%
456 bovine serum albumin (BSA) (Thermo Fisher Scientific) in PBS for 1h, followed by incubation
457 of primary antibody solution diluted in 1% BSA/PBS for 1.5h at RT, 3 washing steps in PBS
458 and subsequent incubation of secondary antibody solution diluted in 1%BSA/PBS for 30 min
459 at RT. Finally, sections were washed three times in PBS, air-dried and mounted using
460 Fluoromount-G with DAPI (Thermo Fisher Scientific). Vibratome sections were blocked in 5%
461 BSA/0.3%Triton- x/PBS for 2h at RT under agitation followed by primary antibody incubation
462 in 1% BSA/0.3%Triton-x/PBS overnight at 4°C under agitation or for 2 days at RT in some
463 cases. The following day sections were washed three times in PBS. In case primary
464 antibodies were not conjugated with a fluorescent dye, samples were incubated with a
465 secondary antibody in 1% BSA/0.3%Triton-x/PBS for 4h at RT under mild agitation and
466 subsequently washed three times in PBS. All samples were then incubated in DAPI solution
467 for 15 min and mounted on a glass slide using Fluoromount-G (Thermo Fisher Scientific).
468 The following primary antibodies were used: α-CD3ε AF488 (17A2)(eBioscience), α-B220-
469 Biotin (RA3-6B2) (eBioscience), α-Collagen IV-Biotin (Abcam), α-CCL21-Biotin (R&D Systems),
470 α-PDPN-Biotin (8.1.1) (eBioscience), α-PDGFR-β (R&D Systems), α-YAP/TAZ (D24E4) (Cell
471 Signal), α-cleaved Caspase 3-AF647 (Asp175) (Cell Signal), α-Ki67-APC (SolA15)
472 (eBioscience), α-ICAM-1 (YN1/1.7.4) (BioXCell), α-VCAM-1 (Phe25-Glu698) (R&D Systems),
473 α-Fibroblast Marker-AF647 (ERTR7) (Santacruz Biotech). α-PNAd (MECA-79) was derived
474 from a concentrated hybridoma supernatant (kind gift from Christine Moussion). The
475 following secondary antibodies were used: Streptavidin-Cy3 (Sigma-Aldrich), Streptavidin-
476 AF647 (Jackson ImmunoResearch), chicken α-goat AF488 (Invitrogen), donkey α-rat AF647
477 (Jackson ImmunoResearch), donkey α-rabbit AF647 (Jackson ImmunoResearch), goat α-
478 mouse IgM AF647 (Invitrogen). Images were acquired on a Zeiss LSM800 inverted confocal
479 laser scanning microscope (CLSM) with the following objectives: 10x/NA0.45, 20x/NA0.8,
480 40x/NA1.2 Water and 63x/NA1.4 Oil Plan-APOCHROMAT.

481 Thick vibratome sections were in some cases cleared using the Ce3D protocol as described
482 previously[51]. Briefly, following antibody-staining samples were washed at RT on a shaker for
483 8h in washing buffer (PBS/0.3% Triton X-100, 0.5% 1-thioglycerol) which was refreshed after
484 4h. Next samples were cleared in freshly prepared Ce3D solution for 2x 1h, mounted in a µ-
485 dishes (Ibidi) and submerged in Ce3D solution. A cover-glass was placed on top to mount
486 cleared samples to the bottom of the well and the dish sealed with parafilm. Large 3D
487 volumes (xy:306x306 µm, z: 50-300 µm) were acquired from Ce3D cleared thick vibratome
488 sections using a spinning-disc microscope (Dragonfly, Andor) with a Apochromat LWD λS
489 40x/1.15 Water 0.60 mm WD objective.

490 **3D LSFM Sample Preparation and Imaging**

491 Terminally anesthetized Ccl19-cre hem; MADM-7$^{GT/TG}$ mice (mix C57BL/6J and CD1
492 background) were *in vivo* stained by retro-orbital injection of 40 µg/PBS mouse α-peripheral
493 node addressin (PNAd) concentrated hybridoma supernatant labeled with Atto-647N-NHS
494 (Atto-Tec). After 10 min, popliteal LNs were harvested and fixed in 4% paraformaldehyde
495 (Electron Microscopy Sciences) overnight at 4°C. Samples were washed in PBS, cleaned
496 under a stereomicroscope and cleared with the CUBIC protocol[52]. Briefly, samples were
497 incubated in CUBIC reagent 1 for 3 days at 37°C, which was replaced every 24h. Samples
498 were then washed with PBS, embedded in 2% low-meting temperature agarose (Sigma-
499 Aldrich), and sequentially dehydrated in 30% sucrose (Sigma-Aldrich) (1 day at 4°C) and 50%
500 sucrose (2 days at 4°C). Finally, samples were incubated in CUBIC reagent 2 for 2 days at RT.
501 Cleared samples were imaged using a custom LSFM setup[53]. Acquired images were stitched
502 using the FIJI Grid/Collection-stitching plugin (Preibitsch Laboratory), despeckled and
503 manually registered using a custom-alignment-tool in Matlab (developed by Ekaterina
504 Papusheva).

505

506 **FRC Cluster Analysis**

507 MADM-labeled cells were detected in 3D by employing a spot detection algorithm (Bitplane
508 Imaris) for each channel (tdTomato & GFP) separately. Chromatic aberrations and the
509 sequential nature of the image acquisition led to a channel misalignment which was
510 corrected for in the following way: the spot coordinates were exported from Imaris and
511 treated as a point cloud for each channel. These point clouds were then registered onto

each other using the Iterative closest point algorithm which corrected the shift and the rotation of the spectral channels. Cells were then sorted into color classes (green (GFP), red (tdTomato) or yellow (double positive) lineage). Red or green, if the spot existed solely in one of the point clouds, or yellow if there were two corresponding spots in both channels that are closer than the typical cell radius.

For the cluster analysis the LN outline and the HEVs were segmented in Imaris using the surface detection feature. To correct errors in the cell detection, falsely detected spots from autofluorescent structures outside of the LN volume were excluded from further analysis. In order to avoid edge effects cells in a region 100 µm from the surface of the analyzed LNs were excluded. FRC clusters were analyzed using a custom Matlab script utilizing a density-based spatial clustering of applications with noise (DBSCAN) algorithm[40] in which FRCs were represented as 3D spheres with a 12 µm diameter. An FRC cluster was defined as a minimum of three FRCs of the same lineage (green or red) within a search-radius of 20 µm from each FRC-sphere's surface.

To generate a random distribution (simulated FRCs), FRC-spheres were placed into the same volume occupied by the real cells and excluded from HEV volumes. For each timepoint the average of 10 distributions was used. The *cluster factor (CF)* was defined as *FRCs in clusters/Total number of FRCs* divided by *Simulated FRCs in clusters/Total number of simulated FRCs*.

FRC Network GAP Analysis

2D: A confocal laser scanning microscope with a 40x 1.2 water-objective (LSM800, Zeiss) was used to acquire image stacks (range 10-30 µm and spaced at 1µm) with a field of view of 240x240 µm and a pixel size of 0.5 µm from T zones in which FRCs were labeled by mGFP (Ccl19-Cre; mTmG mice). These were subsequently segmented using Ilastik software, the result was then transformed into a binary image and noise was removed using a custom FIJI script that utilized the particle detection algorithm. Binarized 3D image-stacks were then used to measure the spacing (gaps) in the network by analyzing the pore-size distribution on individual z-sections. The pore-size distribution was obtained analogously to the pore-size analysis described in *Acton et al.*[22]. Starting with a circle size which corresponded to the

544 maximum gap of the network, circles were consecutively positioned into fitting
545 corresponding gaps of the network. The maximum circle size was determined from a
546 distance transform of the segmented network. Once no more circles of the maximum size
547 could be placed into gaps of the network, the disk size was reduced by one unit and the
548 placement of the disks of reduced sized commenced. This way, the gaps in the network
549 were consecutively filled with circles of decreasing size until the entirety of the gap area was
550 filled. The results were then averaged over the
551 3D: Large 3D volumes (xy:306x306 µm, z:50-500 µm) were acquired from Ce3D[51] cleared
552 thick vibratome sections using a Apochromat LWD λS 40x/1.15 Water 0.60 mm WD
553 objective on a spinning disc microscope (Dragonfly, Andor). Acquired 3D stacks were
554 corrected for fluorescent intensity in z-axis using 'bleach correction (histogram matching)'
555 function in Fiji. Imaris was then used to generate a 3D binary image of the FRC network by
556 utilizing a surface detection feature from the FRC-network fluorescent channel. A custom
557 Matlab script was subsequently used to fit 3D spheres in the 3D gaps of the network analog
558 to the 2D approach.
559
560 **Parallel Plate Compression Experiments**
561 Explanted popliteal LNs were cleaned from adipose tissue under a stereomicroscope and
562 placed on a glass plate within the 37°C, RPMI 1640 (Invitrogen) filled incubation chamber of
563 a MicroSquisher device (CellScale). LNs were oriented to have their long axis along the field
564 of view of the camera. Compression was performed with a glass plate glued onto either a
565 0.304 or 0.408 mm diameter 40 GPa tungsten filament with a length of 60 mm. The glass
566 slide on the compression probe was coated with Poly-HEMA (Sigma-Aldrich) to reduce
567 sticking of the samples. LNs were then compressed by 25% of the initial height by lowering
568 the upper plate down in a timespan of 30 seconds. Lateral side-views of LNs were recorded
569 up to 20-60 min after onset of the experiment, while resistant forces were measured on the
570 upper plate. Compression protocols, images and force acquisition were realized with the
571 SquisherJoy software (CellScale). Length, height, contact area and curvature of LNs were
572 manually measured before compression, and at the equilibrium timepoints using Fiji
573 software. The recorded compression force together with the measured geometrical
574 parameters were used to calculate volumes, Young's modulus, effective resistance and
575 viscosity using a generalized Kelvin model[27]. This was done as following:

The force required to maintain a constant strain of 25% on a LN was measured over time (F(t)). The force initially peaks and then follows a relaxation curve which is fitted by a double exponential decay curve. The simplest way to describe this bimodal dynamic is to incorporate two dashpots with constants μ_1 and μ_2, and two springs with k1 and k2 constants. After 20-60 min, the system reaches an equilibrium where the exerted force by the plate equals the effective resistance of the LN (σ). Therefore, we have:

$$\sigma = \frac{F_{eq}/\pi {R_3}^2}{\left({}^{1}/_{R1} + {}^{1}/_{R2}\right)}$$

where F_{eq} is the equilibrium force at steady state and R1, R2 and R3 are derived from the geometry of the LN.

To obtain the elastic modulus, the stress and strain need to be acquired:

Stress (s) is calculated from the force at equilibrium divided by plate contact area:

$$s = F_{eq}/\pi {R_3}^2$$

and the strain (ε) from:

$$\varepsilon = 1 - \frac{h_{eq}}{h_0}$$

where h_0 and h_{eq} correspond to the initial and equilibrium height of the compressed LN. From here the elastic modulus (E) can be derived:

$$E = s/\varepsilon$$

Next, by fitting a double exponential decay to the force curve we obtain two time-scales, τ_1 and τ_2, where:

$$\tau_i = {}^{\mu_i}/_{k_i} \quad , i = 1, 2$$

Following up on the derivations of the equations as in *Forgacs et al.*[27], μ_1 and μ_2 can be acquired readily, where μ_1 corresponds to the initial fast response in the order of seconds and μ_2 to the slower response in the order of minutes, of which the latter one becomes relevant for the rearrangements of the cells within LNs. Hence, we use μ_2 as our viscosity.

Measurements in which the LN was damaged during preparation (lymphocytes leaking out) or moved/rolled during compression were excluded. In a few cases the viscosity could not be determined (infinitely small) and were also excluded.

LN volumes were calculated from side-view images at *t=0* with the following formula:

$$V = \frac{4}{3}\,\pi\, R1 \left(\frac{h_0}{2}\right)^2$$

599

600 **Micropipette Assay**

601 Popliteal LN explants were cleared from fat and incubated for 10 min in a 2 µg/mL ERTR7-
602 AF647 (Santa-Cruz) in RPMI 1640 (Invitrogen) to label the capsule. LNs were subsequently
603 placed on 3% methylcellulose coated glass bottom Petri dishes (MatTek) in RPMI and kept
604 at 37°C, while imaged on an inverted Leica SP5 microscope using a 20x, 0.7NA objective
605 (Leica Microsystems). The local Young's Modulus of the capsule was measured with a glass
606 micropipette connected to a Microfluidic Flow Control System (Fluigent, Fluiwell), with
607 negative pressure ranging from 7-750 Pa, a pressure accuracy of 7 Pa and change rate of
608 200 $Pa*s^{-1}$. The micropipette equipment was mounted on a motorized micromanipulator
609 (Eppendorf, Transferman Nk2). Both systems were controlled by Dikeria software, Labview
610 (National Instruments). A fire polished micropipette with an inner diameter of 15 µm and
611 flat end (BioMedical instruments) was used for aspiration. The chosen diameter ensured
612 that mainly the capsule was probed and not the underlying parenchyma. While localizing
613 the LN capsule with the micropipette, the pressure inside the micropipette was kept at 0 Pa.
614 For measurements, a negative pressure of 750 Pa was applied, which resulted in the
615 instantaneous aspiration of the capsule. This pressure was chosen as lower pressure
616 regimes did not result in proper aspiration of the capsule. The tongue length of the capsule
617 in the micropipette upon aspiration was manually measured in Fiji from acquired movies.
618 The elasticity was subsequently calculated using the Laplace law:

$$E = \frac{\Delta P}{\left(\frac{h}{d}\right)^2}$$

619 With ΔP being the pressure difference between micropipette and atmosphere, h the height
620 of the measured tongue, and d the micropipette diameter.

621

622 **SEM Sample Preparation and Imaging**

623 Terminally ketamine/xylazine/acepromazine anesthetized mice were transcardially perfused
624 with PB (0.1 M, pH 7.4) and subsequently fixed with 2.5% glutaraldehyde and 2%
625 paraformaldehyde (Science Services) in PB (0.1 M, pH 7.4). LN samples were then dissected
626 and post-fixed in the same buffer for another hour at RT. They were dehydrated in a graded
627 ethanol series of 50%, 70%, 90%, 96%, 100% in H_2O for a minimum of 10 min per step and

628 subsequently kept overnight in fresh 100% ethanol at 4°C. Once in 100% ethanol, samples
629 were dried with a critical point dryer (EM-CPD300, Leica Microsystems), cut in half and
630 coated with a 4nm layer of platinum using a sputter coater (EM-ACE600, Leica
631 Microsystems). The samples were imaged with a field emission scanning electron
632 microscope Merlin compact VP (Carl Zeiss) at 3 kV. The signal was detected by an Everhart-
633 Thornley type secondary electron detector.
634
635 **STEM Tomography Sample Preparation**
636 Alkali maceration of LNs was performed as previously described[54,55]. Briefly, popliteal LNs
637 were isolated from 8–12 weeks old wt C57BL/6 mice and directly fixed in a 2.5%
638 glutaraldehyde and 2% paraformaldehyde in PB (0.1 M, pH 7.4) for a minimum of two weeks
639 at 4°C. Samples were then macerated in aqueous 2.5 M (10% w/v) NaOH solution for 5 days
640 at RT under mild agitation. Next sections were rinsed in H_2O under mild agitation for one to
641 two days until samples became pale. If results were not sufficient, the maceration step was
642 repeated.
643
644 Samples were then treated with 0.5% tannic acid (w/v) in PB (0.1 M, pH 7.4) two times 1h
645 each with freshly prepared solutions, washed in PB and treated with aqueous 1% osmium
646 tetroxide (w/v) for 30 min at 4°C. Samples were contrast enhanced with aqueous 1% uranyl
647 acetate (w/v) overnight at 4°C and Walton´s lead aspartate for 30 min at 60°C. Samples
648 were then dehydrated in graded ethanol, infiltrated with anhydrous propylene oxide and
649 embedded in hard-grade epoxy resin (Durcupan® ACM, Fluca). Samples were consecutively
650 infiltrated with a 3:1 mixture of anhydrous acetone and Durcupan® for 1h at 4°C, 1:1
651 aceton/Durcupan® for 1.5h at 4°C, 1:3 aceton/Durcupan® for 2h at 4°C and mere Durcupan®
652 overnight at RT. Samples were transferred to BEEM capsules (Electron Microscopy
653 Sciences), filled with freshly prepared Durcupan® and cured for 48h at 60°C.
654
655 **STEM Tomography Imaging**
656 Semi-thin sections were cut at 450 nm using an UC7 ultramicrotome (Leica Microsystems)
657 and collected onto formvar-coated 200-line bar grids + 1C/bar (Science Services, G200PB)
658 and coated with evaporated carbon to a thickness of 8nm. Grids were cut in half, mounted
659 on a Half-Mesh High Tilt holder (Jeol, EM-21010/Z09291THTR) and observed under a JEM

2800 scanning transmission electron microscope (Jeol) operated at 200 kV in STEM mode. To compensate for focus, contrast and brightness, and stage shift during image tilt series recording, an automated system was used comprising the STEM Recorder V3 Vers. 3.2.8.0 and the STEM Magica Controller Vers. 0.9.8.1 (both System In Frontier Inc.). Images were collected at 2° intervals between +/-76° of single tilt axis. Magnification was x80k – x600k, image size 512x512 pixels giving a pixel sizes from 6.749463 nm/px to 0.899928 nm/px.

Conduit Stretching Quantification

STEM Tomography images were aligned by cross-correlation and 3D structure of area of interest computed by weighted back-projection using Composer software Vers. 3.0 (System In Frontier Inc.). A 3D Gaussian blur filter and background subtraction (rolling ball algorithm) pre-processing step were performed on the images using FIJI. The 3D image stacks were subsequently loaded into Imaris, and fibrils of conduits were manually traced using the Filament Tracer tool and exported to Matlab format using the Object Exporter (exported from Imaris as filaments). The overall orientation and curvature of the centerline of the entire conduit was approximated by fitting a cubic spline curve with four support points which minimized a hand-crafted cost function through all fibril track data. This cost function penalizes the distance of the desired centerline to the tracks, the total curvature of the centerline and the difference in length between it and the fibril bundles, and ensures that the support points are spaced evenly. In a few cases this spline curve was corrected by hand if it was found to not adequately represent the center line of the bundle. The alignment of the individual fibrils with respect to the centerline of the conduit was calculated as follows: The spline centerline was interpolated in a continuous fashion and the 3D orientation was calculated. Likewise, the tracks of individual fibrils were first smoothed to reduce tracing errors and the 3D orientation of each segment of the trace was calculated. The alignment angle A between the fibril is then given by the angle between the orientation of the segment and the orientation of the centerline at the point that is closest to the segment:

$$A = \operatorname{acos}\left(abs\left(\frac{\vec{v}_{fibril} \cdot \vec{v}_{Centerline}}{\left|\vec{v}_{fibril}\right| \times \left|\vec{v}_{Centerline}\right|} \right) \right)$$

688

689 **UV-Laser Cutter Setup**

690 The UV-laser cutter setup is based on a previously described layout[35,56]. In brief, a passively
691 Q-switched solid-state 355 nm UV-A laser (Powerchip, Teem Photonics) with a repetition
692 rate of 1 kHz, pulse energy of 15 µJ, pulse-length of <350 ps and peak-power of 40 kW was
693 used in conjugation with a spinning disc microscope (Axio Observer Z1, Zeiss). The system is
694 controlled using custom-built software (LabView, National Instruments) enabling cutting in
695 3D. Typically 5% of the power is used to cut tissues.

696

697 **UV-Laser Ablation Experiments**

698 Tension on FRCs, fLECs and capsule ECM was measured by conducting laser ablations on an
699 inverted UV-laser ablation setup with a manufacturer 40x 1.2NA water immersion lens in
700 homeostatic and inflamed LNs. For all experiments 25 UV pulses at 1000 Hz to 40
701 equidistant sites using 200 ms exposure time and frame rate were used to ablate and
702 capture tissue recoil. For FRC and LEC ablation, we established an intravital setup where
703 Ccl19-Cre hem; mTmG hom mice were anesthetized and intact inguinal LNs exposed using a
704 skin flap surgery. The paracortical site of the LN was mounted on a custom-made stage
705 which allowed the LN temperature to be regulated at 37°C. For capsule ECM ablation,
706 popliteal LNs were harvested and incubated in 100 µM TAMRA in RPMI 1640 solution (both
707 Invitrogen) for 15 min at RT and directly used for experiments. Explanted LNs were mounted
708 at room temperature in a glass bottom Petri dish (MatTek) in RPMI and prevented from
709 floating using a 22x22 mm cover glass topping.

710 Cuts were performed in either three z-planes spaced 1 µm apart along a length of either 10
711 µm for FRCs, or in one z-plane along 20 µm for fLECs and capsule ECM. FRC cuts were
712 typically performed at 10-20 µm depth underneath the capsule. Recoil of FRCs and LECs was
713 quantified from kymographs made in FIJI, while capsule ECM recoil was quantified using
714 PIVlab in Matlab. In the latter case, temporal recoil velocities were measured between
715 bandpass filtered pre- and consecutive post-cut frames by averaging the component of the
716 calculated velocity in the perpendicular direction to the cut, within an area of the
717 surrounding cut site.

718

719 **YAP/TAZ Quantification**

720 The nuclear to cytoplasmic ration of stained YAP/TAZ in FRCs were measured from 3D
721 sections of peripheral LNs. In FIJI, FRCs were identified by the mGFP labeling and for each
722 FRC the average YAP/TAZ fluorescent intensity of the nucleus (identified by DAPI) was
723 divided by the average intensity of the adjacent cytoplasm of the cell body. In other cases,
724 YAP/TAZ localization was qualitatively assessed to contain to either contain a higher nuclear
725 or cytoplasmic YAP/TAZ intensity.
726
727 **CCL21 Quantification**
728 Cryosections containing both a control and $FRC^{\Delta TLN1}$ peripheral LN in a single section were
729 stained for CCL21 and pair-wise imaged using similar settings. The average fluorescent
730 intensities of CCL21 were then measured from paracortical areas and normalized to the
731 control.
732
733 **Proliferation and Apoptosis Measurements of FRCs**
734 Large 3D volumes (xy:306x306 µm, z: 50-150 µm) stained for either cleaved Caspase 3 or
735 Ki67 were acquired from Ce3D cleared thick vibratome sections were corrected for
736 fluorescent intensity in z-axis using 'bleach correction (histogram matching)' function in Fiji.
737 Imaris was then used to generate a 3D isosurface of the FRC network by utilizing a surface
738 detection feature from the FRC-network fluorescent channel. The isosurface was then used
739 to mask the cleaved Caspase 3 and Ki67 channels so only the fluorescent signal within the
740 FRC network remained. Positive nuclei were then manually counted from 2D slice views and
741 normalized for per volume unit.
742
743 **Capsule Thickness Measurements**
744 The thickness of capsules was measured in vibratome sections of PROX1-GFP or wt mice,
745 stained for PDGFR-β and DAPI. The size of the capsule was then manually measured in FIJI
746 from the SCS to the surrounding adipose or muscular tissue from at least 3 locations and
747 were averaged per LN.
748
749 **Statistical Analysis**
750 All statistical analyses were performed in GraphPad Prism 8. P-values <0.05 were considered
751 significant.

Software

FIJI	Schindelin et al., 2012	https://fiji.sc/
Imaris	Bitplane	https://imaris.oxinst.com/packages
Excel	Microsoft	https://products.office.com/en-us/?rtc=1
Prism	GraphPad Software	https://www.graphpad.com/scientific-software/prism/
MATLAB	MATLAB Software	https://www.mathworks.com/products/matlab.html
Ilastik	Sommer et al., 2011	https://www.ilastik.org/
SquisherJoy	Cell Scale	https://www.cellscale.com/products/microtester/
Composer software	System In Frontier Inc.	https://temography.com/en/composer-en/
PIVlab	Thielicke and Stamhuis 2014	https://pivlab.blogspot.com/

Data availability

Data supporting the findings of this study are available from the corresponding authors upon.

Code availability

Code used for various analyses in this study are available from the corresponding authors upon request.

References

762

763 1. Lämmermann, T. & Sixt, M. The microanatomy of T-cell responses. *Immunol Rev* **221**, 26–
764 43 (2008).

765 2. Pham, T. H. M., Okada, T., Matloubian, M., Lo, C. G. & Cyster, J. G. S1P1 Receptor
766 Signaling Overrides Retention Mediated by Gαi-Coupled Receptors to Promote T Cell Egress.
767 *Immunity* **28**, 122–133 (2008).

768 3. Druzd, D. *et al.* Lymphocyte Circadian Clocks Control Lymph Node Trafficking and
769 Adaptive Immune Responses. *Immunity* **46**, 120–132 (2017).

770 4. Suzuki, K., Hayano, Y., Nakai, A., Furuta, F. & Noda, M. Adrenergic control of the adaptive
771 immune response by diurnal lymphocyte recirculation through lymph nodes. *J Exp Med* **213**,
772 2567–2574 (2016).

773 5. Luther, S. A., Tang, H. L., Hyman, P. L., Farr, A. G. & Cyster, J. G. Coexpression of the
774 chemokines ELC and SLC by T zone stromal cells and deletion of the ELC gene in the plt/plt
775 mouse. *Proc National Acad Sci* **97**, 12694–12699 (2000).

776 6. Matloubian, M. *et al.* Lymphocyte egress from thymus and peripheral lymphoid organs is
777 dependent on S1P receptor 1. *Nature* **427**, 355–360 (2004).

778 7. Mionnet, C. *et al.* High endothelial venules as traffic control points maintaining
779 lymphocyte population homeostasis in lymph nodes. *Blood* **118**, 6115–6122 (2011).

780 8. Andrian, U. H. von & Mempel, T. R. Homing and cellular traffic in lymph nodes. *Nat Rev*
781 *Immunol* **3**, 867–878 (2003).

782 9. Link, A. *et al.* Fibroblastic reticular cells in lymph nodes regulate the homeostasis of naive
783 T cells. *Nat Immunol* **8**, 1255–1265 (2007).

784 10. Knop, L. *et al.* IL-7 derived from lymph node fibroblastic reticular cells is dispensable for
785 naive T cell homeostasis but crucial for central memory T cell survival. *Eur J Immunol* **50**,
786 846–857 (2020).

787 11. Gorelik, L. *et al.* Normal B Cell Homeostasis Requires B Cell Activation Factor Production
788 by Radiation-resistant Cells. *J Exp Medicine* **198**, 937–945 (2003).

789 12. Cremasco, V. *et al.* B cell homeostasis and follicle confines are governed by fibroblastic
790 reticular cells. *Nat Immunol* **15**, 973–981 (2014).

791 13. Nakai, A., Hayano, Y., Furuta, F., Noda, M. & Suzuki, K. Control of lymphocyte egress
792 from lymph nodes through β2-adrenergic receptors. *J Exp Med* **211**, 2583–2598 (2014).

14. Devi, S. *et al.* Adrenergic regulation of the vasculature impairs leukocyte interstitial migration and suppresses immune responses. *Immunity* **54**, 1219-1230.e7 (2021).

15. Kaldjian, E. P., Gretz, J. E., Anderson, A. O., Shi, Y. & Shaw, S. Spatial and molecular organization of lymph node T cell cortex: a labyrinthine cavity bounded by an epithelium-like monolayer of fibroblastic reticular cells anchored to basement membrane-like extracellular matrix. *Int Immunol* **13**, 1243–1253 (2001).

16. Sixt, M. *et al.* The Conduit System Transports Soluble Antigens from the Afferent Lymph to Resident Dendritic Cells in the T Cell Area of the Lymph Node. *Immunity* **22**, 19–29 (2005).

17. Bajénoff, M. *et al.* Stromal Cell Networks Regulate Lymphocyte Entry, Migration, and Territoriality in Lymph Nodes. *Immunity* **25**, 989–1001 (2006).

18. Perez-Shibayama, C., Gil-Cruz, C. & Ludewig, B. Fibroblastic reticular cells at the nexus of innate and adaptive immune responses. *Immunol Rev* **289**, 31–41 (2019).

19. Krishnamurty, A. T. & Turley, S. J. Lymph node stromal cells: cartographers of the immune system. *Nat Immunol* **21**, 369–380 (2020).

20. Yang, C.-Y. *et al.* Trapping of naive lymphocytes triggers rapid growth and remodeling of the fibroblast network in reactive murine lymph nodes. *Proc National Acad Sci* **111**, E109–E118 (2014).

21. McConnell, I. & Hopkins, J. Lymphocyte traffic through antigen-stimulated lymph nodes. I. Complement activation within lymph nodes initiates cell shutdown. *Immunology* **42**, 217–23 (1981).

22. Acton, S. E. *et al.* Dendritic cells control fibroblastic reticular network tension and lymph node expansion. *Nature* **514**, 498–502 (2014).

23. Astarita, J. L. *et al.* The CLEC-2–podoplanin axis controls the contractility of fibroblastic reticular cells and lymph node microarchitecture. *Nat Immunol* **16**, 75–84 (2015).

24. Chyou, S. *et al.* Coordinated Regulation of Lymph Node Vascular–Stromal Growth First by CD11c+ Cells and Then by T and B Cells. *J Immunol* **187**, 5558–5567 (2011).

25. Gregory, J. L. *et al.* Infection Programs Sustained Lymphoid Stromal Cell Responses and Shapes Lymph Node Remodeling upon Secondary Challenge. *Cell Reports* **18**, 406–418 (2017).

26. Majumder, S. *et al.* IL-17 metabolically reprograms activated fibroblastic reticular cells for proliferation and survival. *Nat Immunol* **20**, 534–545 (2019).

27. Forgacs, G., Foty, R. A., Shafrir, Y. & Steinberg, M. S. Viscoelastic Properties of Living Embryonic Tissues: a Quantitative Study. *Biophys J* **74**, 2227–2234 (1998).

826 28. Delarue, M. *et al.* Self-driven jamming in growing microbial populations. *Nat Phys* **12**,
827 762–766 (2016).

828 29. Jain, R. K., Martin, J. D. & Stylianopoulos, T. The Role of Mechanical Forces in Tumor
829 Growth and Therapy. *Annu Rev Biomed Eng* **16**, 321–346 (2014).

830 30. Mao, Y. *et al.* Differential proliferation rates generate patterns of mechanical tension
831 that orient tissue growth. *Embo J* **32**, 2790–2803 (2013).

832 31. Gallatin, W. M., Weissman, I. L. & Butcher, E. C. A cell-surface molecule involved in
833 organ-specific homing of lymphocytes. *Nature* **304**, 30–34 (1983).

834 32. Chai, Q. *et al.* Maturation of Lymph Node Fibroblastic Reticular Cells from
835 Myofibroblastic Precursors Is Critical for Antiviral Immunity. *Immunity* **38**, 1013–1024
836 (2013).

837 33. Madisen, L. *et al.* A robust and high-throughput Cre reporting and characterization
838 system for the whole mouse brain. *Nat Neurosci* **13**, 133–140 (2010).

839 34. Smutny, M., Behrndt, M., Campinho, P., Ruprecht, V. & Heisenberg, C.-P. Tissue
840 Morphogenesis, Methods and Protocols. *Methods Mol Biology* **1189**, 219–235 (2014).

841 35. Colombelli, J., Grill, S. W. & Stelzer, E. H. K. Ultraviolet diffraction limited nanosurgery of
842 live biological tissues. *Rev Sci Instrum* **75**, 472–478 (2004).

843 36. Panciera, T., Azzolin, L., Cordenonsi, M. & Piccolo, S. Mechanobiology of YAP and TAZ in
844 physiology and disease. *Nat Rev Mol Cell Bio* **18**, 758–770 (2017).

845 37. Zong, H., Espinosa, J. S., Su, H. H., Muzumdar, M. D. & Luo, L. Mosaic Analysis with
846 Double Markers in Mice. *Cell* **121**, 479–492 (2005).

847 38. Contreras, X. *et al.* A genome-wide library of MADM mice for single-cell genetic mosaic
848 analysis. *Cell Reports* **35**, 109274 (2021).

849 39. Hippenmeyer, S., Johnson, R. L. & Luo, L. Mosaic Analysis with Double Markers Reveals
850 Cell-Type-Specific Paternal Growth Dominance. *Cell Reports* **3**, 960–967 (2013).

851 40. Ester, M., Kriegel, H.-P., Sander, J. & Xu, X. A density-based algorithm for discovering
852 clusters in large spatial databases with noise. in *Proceedings of the Second International*
853 *Conference on Knowledge Discovery and Data Mining* (eds. Simoudis, E., Han, J. & Fayyad,
854 U.) 226–231 (AAAI Press, 1996).

855 41. Bailey, N. T. J. *The Elements of Stochastic Processes with Applications to the Natural*
856 *Sciences*. (Wiley-Interscience, 1990).

857 42. Schaeuble, K. *et al.* Perivascular Fibroblasts of the Developing Spleen Act as LTα1β2-
858 Dependent Precursors of Both T and B Zone Organizer Cells. *Cell Reports* **21**, 2500–2514
859 (2017).

860 43. Cheng, H.-W. *et al.* Origin and differentiation trajectories of fibroblastic reticular cells in
861 the splenic white pulp. *Nat Commun* **10**, 1739 (2019).

862 44. Austen, K. *et al.* Extracellular rigidity sensing by talin isoform-specific mechanical
863 linkages. *Nat Cell Biol* **17**, 1597–1606 (2015).

864 45. Martinez, V. G. *et al.* Fibroblastic Reticular Cells Control Conduit Matrix Deposition
865 during Lymph Node Expansion. *Cell Reports* **29**, 2810-2822.e5 (2019).

866 46. Choi, S. Y. *et al.* YAP/TAZ direct commitment and maturation of lymph node fibroblastic
867 reticular cells. *Nat Commun* **11**, 519 (2020).

868 47. Kumar, V. *et al.* A Dendritic-Cell-Stromal Axis Maintains Immune Responses in Lymph
869 Nodes. *Immunity* **42**, 719–730 (2015).

870 48. Jarjour, M. *et al.* Fate mapping reveals origin and dynamics of lymph node follicular
871 dendritic cells. *J Exp Med* **211**, 1109–1122 (2014).

872 49. Mills, S. *Histology for Pathologists*. (LWW, 2019).

873 50. Nieswandt, B. *et al.* Loss of talin1 in platelets abrogates integrin activation, platelet
874 aggregation, and thrombus formation in vitro and in vivo. *J Exp Medicine* **204**, 3113–3118
875 (2007).

876 51. Li, W., Germain, R. N. & Gerner, M. Y. High-dimensional cell-level analysis of tissues with
877 Ce3D multiplex volume imaging. *Nat Protoc* **14**, 1708–1733 (2019).

878 52. Susaki, E. A. *et al.* Whole-Brain Imaging with Single-Cell Resolution Using Chemical
879 Cocktails and Computational Analysis. *Cell* **157**, 726–739 (2014).

880 53. Abe, J. *et al.* Light sheet fluorescence microscopy for in situ cell interaction analysis in
881 mouse lymph nodes. *J Immunol Methods* **431**, 1–10 (2016).

882 54. OHTANI, O. Three-dimensional Organization of the Connective Tissue Fibers of the
883 Human Pancreas: A Scanning Electron Microscopic Study of NaOH Treated-Tissues. *Arch*
884 *Histol Japon* **50**, 557–566 (1987).

885 55. Ushiki, T., Ohtani, O. & Abe, K. Scanning electron microscopic studies of reticular
886 framework in the rat mesenteric lymph node. *Anatomical Rec* **241**, 113–122 (1995).

887 56. Behrndt, M. *et al.* Forces Driving Epithelial Spreading in Zebrafish Gastrulation. *Science*
888 **338**, 257–260 (2012).

889

Acknowledgements

This research was supported by the Scientific Service Units of IST Austria through resources provided by the Bio Imaging, Electron Microscopy, Preclinical and Life Science Facilities. We thank Christine Moussion for providing anti-PNAd antibody, Simon Hippenmeyer and David Critchley for respectively donating transgenic MADM-7 and Talin1floxed mice, and Ekaterina Papusheva for providing a custom 3D channel alignment script. This work was supported by European Research Council grant ERC-CoG-72437.

Contributions

F.P.A. designed experiments, and performed all *in vivo* and *ex vivo* experiments with assistance of M.H., M.B., S.S and G.K.; J.A. cleared samples and did light-sheet imaging, F.P.A. did all other fluorescent imaging. W.A.K. processed samples for electron tomography, and W.A.K., T.C. and F.P.A. acquired tomograms. F.P.A. did all data processing and analysis with help of R.H., S.S. and G.K; R.H. wrote all custom analysis scripts. S.H. and E.H. aided in the interpretation of MADM and mechanical data, respectively. S.L discussed data. M.S. directed the study, F.P.A. and M.S. wrote the manuscript, and all authors critically reviewed the manuscript.

Ethics declarations

The authors declare no competing interests.

906 **Figure 1.** The reactive lymph node resists swelling. (**a**) Side-view focus-stack of popliteal LNs
907 in homeostasis (D0) and inflammation (D14). Scale bar = 500 µm. (**b**) Volumes of swelling
908 LNs calculated from 2D-side views over the course of two-week following onset of
909 immunization. Means±SEM are connected (blue line) and a linear regression line (dashed)
910 has been fitted to the data. (**c-d**) Overview of the stress-relaxation experiment on explanted
911 popliteal LNs (D2 of inflammation depicted). (**c**) Measured geometrical parameters are
912 annotated on 2D-side images acquired during a measurement. Scale bar = 300 µm. (**d**) The
913 stress relaxation curve is given by the measured force over time from which the equilibrium
914 force (long timescale) parameter), viscosity (medium timescale) and Young's Modulus (short
915 timescale) relaxation parameters are derived. (**e-g**) Quantification of tissue properties in
916 homeostasis (D0) and inflammation (D2, D4, D8, D14) derived from the stress relaxation
917 curve and geometrical properties. Each datapoint represents a single measured LN.
918 Measurements are pooled from LNs harvested from at least 5 mice and multiple
919 experiments. Mean±SEM. (**e**) Quantification of the effective resistance. (**f**) Quantification of
920 the viscosity. (**g**) Quantification of the Young's Modulus. For statistical analysis see
921 Supplementary Information, table 1. *P<0.05, **P<0.01, ****P<0.0001.
922
923 **Figure 2**. Lymphocyte numbers generate pressure and drive lymph node swelling. (**a-j**)
924 Analysis of stress-relaxation experiments on explanted LNs. Each datapoint represents a
925 single measured LN. Measurements are pooled from LNs harvested from at least 5 mice and
926 multiple experiments. Mean±SEM are given. (**a**) Side-view of explanted homeostatic LNs
927 from mice treated with anti-CD62L or PBS. Scale bars = 300 µm. Dashed lines depict the
928 outline of LNs. (**b**) Quantification of LN volume. (**c**) Quantification of the effective resistance.
929 (**d**) Quantification of the viscosity. (**e**) Quantification of the Young's Modulus. (**f**) Side-view of
930 explanted D4 inflamed LNs from wt and OTII mice treated with anti-CD62L or PBS. Scale bars
931 = 400 µm. Dashed lines depict the outline of LNs. (**g**) Quantification of LN volumes. (**h**)
932 Quantification of the effective resistance. (**i**) Quantification of the tissue viscosity. (**j**)
933 Quantification of the Young's Modulus. For statistical analysis see Supplementary
934 Information, table 1. ns, not significant. ns, not significant. *P<0.05, **P<0.01, ***P<0.001,
935 ****P<0.0001.
936

937 **Figure 3.** The FRC network stretches upon lymph node swelling. (**a**) Overview of the FRC
938 network gap analysis. Left: mGFP labeled FRCs (green), middle: segmented FRC network
939 (white), right: gaps (randomly colored circles) in the FRC network. Scale bar = 20 µm. (**b**)
940 Representative images of FRC networks gaps in homeostasis (D0) and inflammation (D2, D4,
941 D8 and D14). (**c**) Averaged and smoothed distribution of FRC network fitted circle
942 distribution plotted as the Weighted Area Fraction as a function of the fitted circle diameter.
943 (**d**) Quantification of the mean fitted-circle diameter. Each datapoint represents the average
944 value of 10-30 analyzed consecutive sections of an acquired 3D volume. Means for each
945 timepoint are depicted as a black line. Data are for each timepoint pooled from 5 popliteal
946 or inguinal LNs from at least 3 mice and 2 separate experiments. For statistical analysis see
947 Supplementary Information, table 1. ***P<0.001, ****P<0.0001.
948
949 **Figure 4.** Conduits are stretched in the swelling lymph node. (**a**) Overview of STEM
950 tomography acquisition of macerated LN samples. Images show the fibrillar collagen of T
951 zone conduits at a single tilt angle, and a maximum intensity projection crop of a 3D conduit
952 reconstructed from multiple tilting angles. (**b**) Representative 3D reconstructions of fibrillar
953 collagen (blue) from macerated conduits at homeostasis (day 0) and inflammation (D2, D4
954 and D14) in which the conduit center line (yellow) and tracked fibril segments (grey) are
955 annotated. (**c**) Visual representation of the conduit fibril alignment analysis of an imaged 3D
956 conduit volume. Angles of individual fibril segments (thick colored lines) with the center line
957 of the conduit (dashed black line) are measured at multiple points along the fibril segment
958 (thin colored lines) and averaged per fibril segment. (**d**) Quantification of conduit fibril
959 alignment with center line. Each datapoint represents an individual fibril segment. Means
960 are depicted as black lines. For statistical analysis see Supplementary Information, table 1.
961 ns, not significant. ***P<0.001, ****P<0.0001.
962
963 **Figure 5.** FRC network tension increases upon lymph node swelling. (**a**) Overview of *in vivo*
964 UV-laser cut experiment of the FRC network. Inguinal LNs from FRC-mGFP mice are
965 surgically exposed and kept hydrated at 37°C. A high UV-laser cuts the FRC network along 10
966 µm at 3 different planes after which the local recoil of the FRC network is imaged. Scissor
967 and line indicate cutting location and arrows the recoiling FRC network. Scale bars = 20 µm.
968 (**b**) Representative example of FRC network recoil. Images depict stills from before (t=-1s),

969 directly after (t=0s) and late after (t=6.2s) cutting (scale bars = 5 µm), with corresponding
970 kymograph along the recoil axis (scale bar x-axis = 1s, y-axis = 2 µm). Scissor and line
971 indicate cutting location and arrows the recoiling FRC network. Dashed lines in kymograph
972 indicate slopes used to calculate the recoil velocity, and vertical white line the cut. (**c**)
973 Quantification of recoil velocity from kymographs. Each datapoint represents a single FRC
974 network cut. Data is pooled from 3-4 animals and at least 2 experiments per analyzed
975 timepoint. Means±SEM are depicted and connected with a line. (**d**) 3D view of the FRC
976 network and stained for YAP/TAZ. Stack size 20 µm. Scale bar = 20 µm. (**e**) Representative
977 examples of YAP/TAZ nuclear and cytoplasmic localization. N:C = nuclear to cytoplasmic
978 fluorescent intensity ratio. (**f**) Quantification of YAP/TAZ N:C ratio. Dashed line indicates an
979 equal ratio. Each datapoint corresponds to a single measured FRC. Measurements are taken
980 from a total of 3 LNs per analyzed timepoint from at least two separate experiments.
981 Means±SEM are depicted and connected with a line. For statistical analysis see
982 Supplementary Information, table 1. ns, not significant. *P<0.05, **P<0.001, ****P<0.0001.
983
984 **Figure 6**. FRCs in the swelling lymph node undergo distributed clonal expansion. (**a**)
985 Schematic overview of the sparse mosaic analysis with double markers (MADM) labeling
986 approach for FRC cluster imaging. (**b-k**) Quantification of light sheet images from cleared
987 LNs in homeostasis (D0) and inflammation (D4 and D8). All graphs depict the mean±SD. Each
988 datapoint represents a single popliteal LN. LNs are retrieved from at least 3 mice and 2
989 separate experiments for each condition. (**b**) LN volumes. (**c**) Numbers of MADM labeled
990 FRCs. (**d**) Numbers of FRCs found in clusters. (**e**) Number of clusters. (**f**) 3D view of HEVs
991 (grey) and smoothed convex-hull of cluster volumes (randomly colored) in a homeostatic
992 (D0) and inflamed (D4) LN, scale bar = 200 µm (**g**) Frequency distribution of FRC cluster sizes
993 found in observed and simulated data in homeostasis (D0) and inflammation (D4 and D8).
994 (**h**) Quantification of the cluster factor (CF) between homeostatic (D0) and inflamed LNs (D4
995 and D8). (**i**) Number of FRC clusters in homeostatic (D0) and inflamed LNs (D4 and D8)
996 plotted as a function of the distance from the nearest HEV. (**j**) Correlation-matrix of paired
997 variables assessed in the cluster analysis. Spearman correlation: *p*-values are given and the
998 correlation-coefficients are color-coded. (**k**) CF plotted as a function of the LN volume. A
999 spline-fit is plotted through the data-points. For statistical analysis see Supplementary
1000 Information, table 1. ns, not significant. **P<0.01, ***P<0.001, ****P<0.0001.

1001

1002

1003 **Figure 7.** Talin1 is required for FRC mechanosensing. (**a**) Quantification of LN weights in
1004 homeostasis and following inflammation (D4 and D14) in control and FRC$^{\Delta Talin1}$ mice. Each
1005 datapoint represents a single LN. Data is pooled from at least 5 mice from multiple
1006 experiments per condition. Insert depicts the grow curves of the plotted data fitted with a
1007 non-linear regression function. Mean±SEM. (**b**) T zone FRC network of FRC-mGFP (control)
1008 and FRC$^{\Delta Talin1}$-GFP mice stained for YAP/TAZ. Enlargements depict representative examples
1009 of the N:C of YAP/TAZ. Scale bars = 10 µm. (**c**) Quantification of YAP/TAZ localization in FRCs
1010 of control and FRC$^{\Delta Talin1}$ mice in homeostasis (D0) and at inflammation (D4). Mean±SEM. (**d**)
1011 Representative 3D images of 3D network analysis of control and FRC$^{\Delta Talin1}$ mice in
1012 homeostasis (D0) and following inflammation (D4 and D14). Imaged stack size: 100-300 µm.
1013 Scale bars = 50 µm. (**e**) Quantification of FRC network analysis as shown in **d**. Left: average
1014 weighted volume fraction plotted as function of the sphere diameter. Right: average sphere
1015 diameter for all conditions. Each datapoint represents an individual LN from at least 3 mice
1016 and 2 experiments per condition. Means are depicted by black lines. (**f**) Quantification of
1017 cleaved Caspase3+ FRCs from FRC-mGFP (control) and FRC$^{\Delta Talin1}$-GFP mice in homeostasis
1018 (D0) and inflammation (D4 and D8). Each datapoint represents a single LN. Data pooled
1019 from 3 mice per timepoint. Images depict the identification of an apoptotic FRC. Scale bar =
1020 3 µm. (**g**) Quantification of Ki67+ FRCs from FRC-mGFP (control) and FRC$^{\Delta Talin1}$-GFP mice in
1021 homeostasis (D0) and inflammation (D4 and D8). Each datapoint represents a single LN.
1022 Images depict the identification of a proliferating FRC. Scale bar = 3 µm. Data pooled from 3
1023 mice per timepoint. Mean±SD. For statistical analysis see Supplementary Information, table
1024 1. ns, not significant. *P<0.05, **P<0.01, ***P<0.001, ****P<0.0001.

1025

1026 **Figure 8.** Capsule fibrosis constrains lymph nodes at late timepoints. (**a**) Overview of
1027 intravital UV-laser cut experiments of the SCS fLECs. Inguinal LNs from FRC-mGFP mice, in
1028 which SCS fLECs are sparsely labeled with a mGFP are surgically exposed. A high UV-laser
1029 cuts the cell along 20 µm in one plane after which the local recoil is imaged. Images depict
1030 stills from before (t=-1s), directly after (t=0s) and late after (t=10.2s) cutting (scale bars = 5
1031 µm), with corresponding kymograph along the recoil axis (scale bar x-axis = 1s, y-axis = 2
1032 µm). Scissor and line indicate location of cut and arrows the recoiling cell. Dashed lines in

1033 kymograph indicate slopes used to calculate the recoil velocity, and vertical white line the
1034 cut. (**b**) Quantification of experiments as described in **a** for homeostatic (D0) and inflamed
1035 (D2, D4, D8, D14) LNs. Each datapoint represents a recoil-measurement of a single fLEC.
1036 Data pooled from 3 mice and at least two experiments. Mean±SEM are depicted and
1037 connected with a line. (**c**) Representative confocal images of LN capsules from PROX1-GFP
1038 mice in homeostasis (D0) and inflammation (D4, D8 and D14), in which LECs are labeled by a
1039 cytoplasmic GFP. Mesenchymal cells are stained for PDGFR-β, and nuclei are counterstained
1040 with DAPI. Scale bars = 20 µm. (**d**) Quantification of the capsule thickness measured from
1041 the SCS as depicted in **c.** Each datapoint represents the average of 3 measurements per LN.
1042 Mean±SEM are connected with a line. Data pooled from 5 LNs derived from 3 mice per
1043 timepoint. (**e**) Overview of micro-pipette assay for capsule stiffness measurements.
1044 Capsules of explanted popliteal LNs are labeled by brief incubation with Alexa Fluor 647-
1045 conjugated anti-ERTR7 antibody, upon which a small diameter glass pipette is placed on the
1046 capsule and a defined negative pressure applied. The ECM 'tongue' entering the pipette is
1047 subsequently measured. The local effective Young's Modulus of the capsule is derived using
1048 Laplace's law. Scale bar = 50 µm. (**f**) Quantification of measurements as described in **e** for
1049 homeostatic (D0) and inflamed (D2, D4, D8 and D14) LNs. Each datapoint represents the
1050 average of 3 measurements per LN. Mean±SEM are connected with a line. Data pooled from
1051 5 LNs derived from 3 mice per timepoint. (**g**) Quantification of the Capsule swelling
1052 resistance as measured by the Passive Tension, given by multiplying the capsule thickness
1053 and Young's modulus from **d** and **f**, respectively. Each datapoint represents a single LN.
1054 Mean±SEM are connected with a line. (**h**) Schematic of the mechanical dynamics of the
1055 swelling LN. For statistical analysis see Supplementary Information, table 1. ns, not
1056 significant. **P<0.01, ***P<0.001.

1057 **Supplementary Figure 1.** (**a**) Quantification of popliteal LN volumes calculated from 2D side
1058 views in homeostasis (D0) and inflammation (D2, D4, D8, D14) acquired from parallel plate
1059 compression experiments. Mean±SEM. (**b**) Relation between calculated volumes and
1060 measured weights of popliteal LNs in homeostasis and inflammation. A regression line is
1061 fitted. (**c**) Example of a double-exponential force fit (red line) on a stress-relaxation
1062 measurement. Arrow indicates the force at equilibrium (F_{eq}). (**d**) Average of stress-relaxation
1063 curves for all measured conditions. Mean±SEM. (**e**) Schematic representation of the

1064 generalized Kelvin model and formulas used to calculate tissue properties from parallel
1065 plate stress-relaxation experiments. Adapted from *Forgacs et al.*. (**f**) SEM image of packed
1066 lymphocytes in the LN paracortex. Scale bar = 2 µm. For statistical analysis see
1067 Supplementary Information, table 1. **P<0.01, ****P<0.0001.

1068 **Supplementary Figure 2.** (**a**) Schematic of LN processing for STEM tomography of T zone
1069 conduits. (**b**) Example of a macerated conduit imaged by STEM in which the characteristic D-
1070 period of collagen fibrils can be observed. Scale bar = 500 µm. (**c**) Examples of a T zone
1071 conduit at different tilting angles acquired by STEM tomography. (**d**) Schematic of a
1072 computed weight back projection to reconstruct a 3D volume of a conduit from differential
1073 tilting angles.

1074 **Supplementary Figure 3.** (**a**) Schematic of the MADM labeling principle. Rare
1075 interchromosomal recombination in the G2 cell cycle phase following x-segregation of
1076 chromosomes labels FRCs with either a cytoplasmic tdTomato or GFP. (**b**) Sparse labeling of
1077 FRCs. Scale bar = 200 µm. (**c**) 3D fluorescent intensity images of GFP labeled FRCs and *in situ*
1078 labeled HEVs by anti-PNAd-ATTO647n antibody. (**d**) Quantification of the MADM labeling
1079 distribution in homeostasis (D0) and inflammation (D4 and D8). Each datapoint represents a
1080 single LN. Mean±SD. (**e**) Overview of the labeling of HEVs and mapping of labeled FRCs (only
1081 tdTomato+FRCs are shown) at D4 of inflammation. The enlarged image depicts the mapping
1082 of individual FRCs by a grey sphere at the center of each cell. Scale bars = 200 µm. (**f**)
1083 Formula for the calculation of the cluster factor (CF) per LN. (**g**) Quantification of the
1084 average distance to the nearest neighbor (NN) of both mapped FRCs and randomly localized
1085 FRCs from simulations in homeostasis (D0) and inflammation (D4 and D8). Means are
1086 depicted by black lines. (**h**) Quantification of relative numbers of MADM-labeled FRCs found
1087 in clusters in both homeostasis (D0) and inflammation (D4 and D8). Mean±SD. For statistical
1088 analysis see Supplementary Information, table 1. ns, not significant. **P<0.01, ***P<0.001.

1089 **Supplementary Figure 4.** (**a**) Quantification of steady-state popliteal and inguinal LN weights
1090 from control and $FRC^{\Delta Talin1}$ mice. Each datapoint represents a measured LN. Images show a
1091 representative inguinal LN for each condition. Scale bars = 1 mm. (**b**) Quantification of
1092 steady-state T zone CCL21 protein as measured *in situ* by fluorescent intensity following
1093 staining for CCL21. Measurements are taken from histological sections from 5 LNs of 3 mice

1094 for each condition. Mean±SEM. Scale bars = 20 µm. (**c**) T zone and B-cell follicles in steady-
1095 state popliteal LNs from control and FRC$^{\Delta Talin1}$ mice stained for CD3 (T cells) and B220 (B
1096 cells). Scale bars = 200 µm. (**d**) ICAM-1, PDPN, VCAM and merged staining from steady-state
1097 popliteal LN T zones from control and FRC$^{\Delta Talin1}$ mice. Scale bars = 20 µm. (**e**) Overview of
1098 the T zone FRC network in homeostasis (D0) and inflammation (D4 and D14) between FRC-
1099 mGFP (control) and FRC$^{\Delta Talin1}$-mGFP mice stained for collagen IV. Scale bar = 50 µm. For
1100 statistical analysis see Supplementary Information, table 1. *P<0.05, ****P<0.0001.

1101 **Supplementary Figure 5.** (**a**) Ccl19-Cre; mTmG mice sparsely label fLECs of the SCS. Zoomed
1102 window depict the SCS with LECs brightly labeled with tdTomato (mTdT) and the sparsely
1103 labeled fLEC (mGFP), given by the double positive labeling with the fLEC-marker LYVE-1
1104 (gray). (**b**) Overview of the UV-laser cut experiment on TAMRA labeled capsule ECM of
1105 explanted LNs in homeostasis (D0) and inflammation (D2, D4, D8, D14), which faithfully
1106 represents capsule ECM as observed in alkali macerated LNs imaged by STEM and SEM.
1107 Particle imaging velocimetry (PIV) was used to measure displacement of structures above
1108 and below the cut site from band-pass filtered images. Recoil displacement is depicted by
1109 orange vectors. Scale bar STEM image = 5 µm, SEM image = 1 µm, fluorescent TAMRA-
1110 labeled image = 20 µm. (**c**) Quantification of recoil velocities of capsule cuts from
1111 experiments on homeostatic (D0) and inflamed (D2, D4, D8, D14) LNs as described in **b**. Each
1112 datapoint represents a single cut. Between 14 and 24 cuts were taken per measured
1113 timepoint from at least 5 LNs from two animals and at least two separate experiments.
1114 Mean+SEM connected by a line. (**d**) Representative histological examples of LN capsules
1115 from PROX1-GFP mice in homeostasis and D14 of inflammation, stained for PDGFR-β and
1116 counterstained with DAPI. Scale bars = 200 µm. For statistical analysis see Supplementary
1117 Information, table 1. *P<0.05, **P<0.01.

1118 **Supplementary Movie 1.** Example of low (homeostasis; D0) and high tension (Inflammation;
1119 D4) of the FRC network as given by the recoil speed following *in vivo* UV-laser cutting in
1120 surgically exposed inguinal LNs of FRC-mGFP mice.

Figure 1

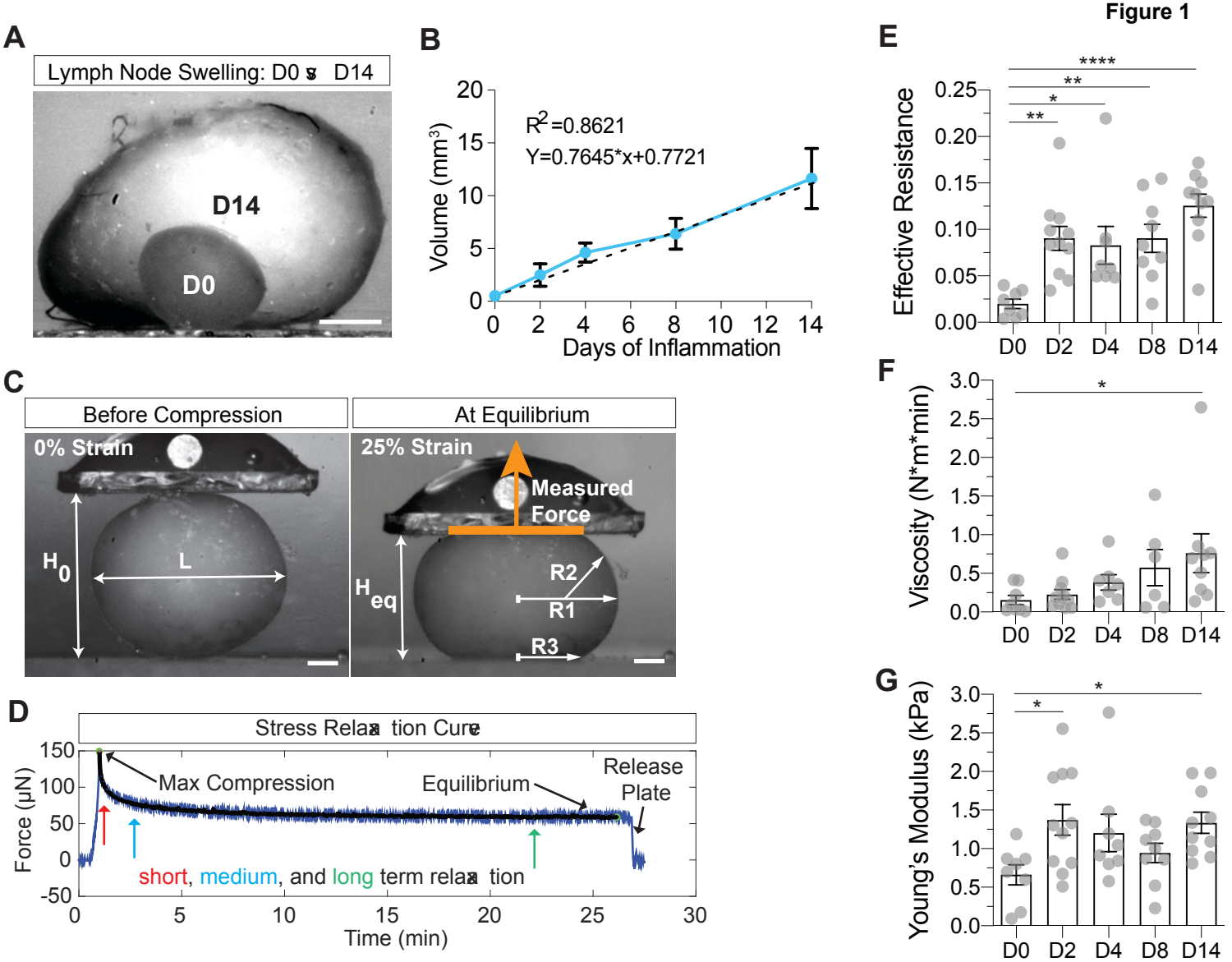
A
Lymph Node Swelling: D0 vs D14
D14
D0
B
R^2=0.8621
Y=0.7645*x+0.7721
Volume (mm³)
Days of Inflammation
C
Before Compression
At Equilibrium
0% Strain
25% Strain
Measured Force
H_0
L
H_{eq}
R2
R1
R3
D
Stress Relaxation Curve
Max Compression
Equilibrium
Release Plate
short, medium, and long term relaxation
Force (μN)
Time (min)
E
Effective Resistance
D0
D2
D4
D8
D14
F
Viscosity (N*m*min)
G
Young's Modulus (kPa)

Figure 2

Homeostasis

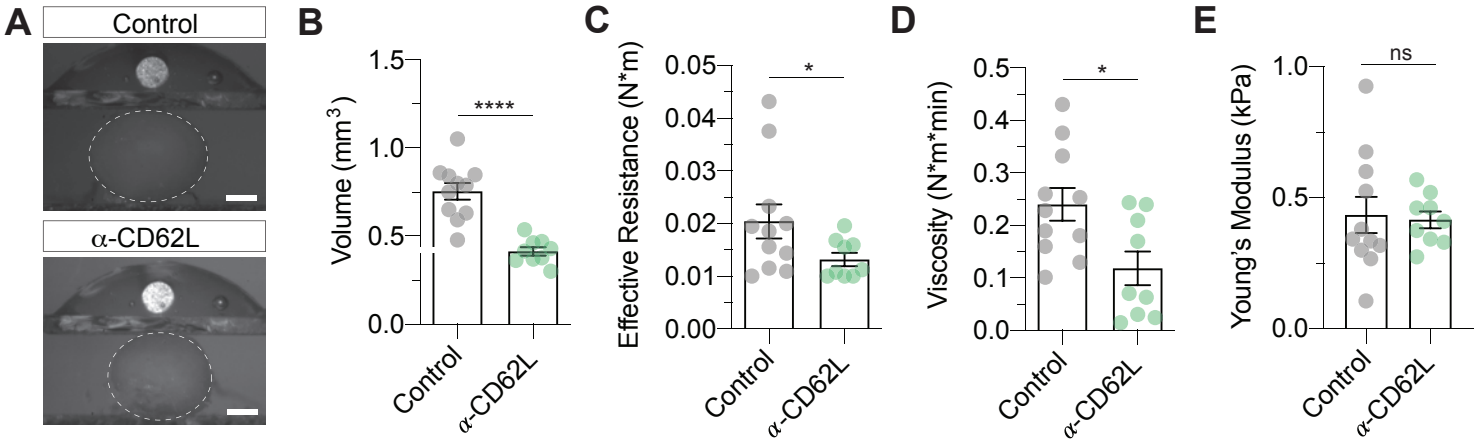

Inflammation Day 4

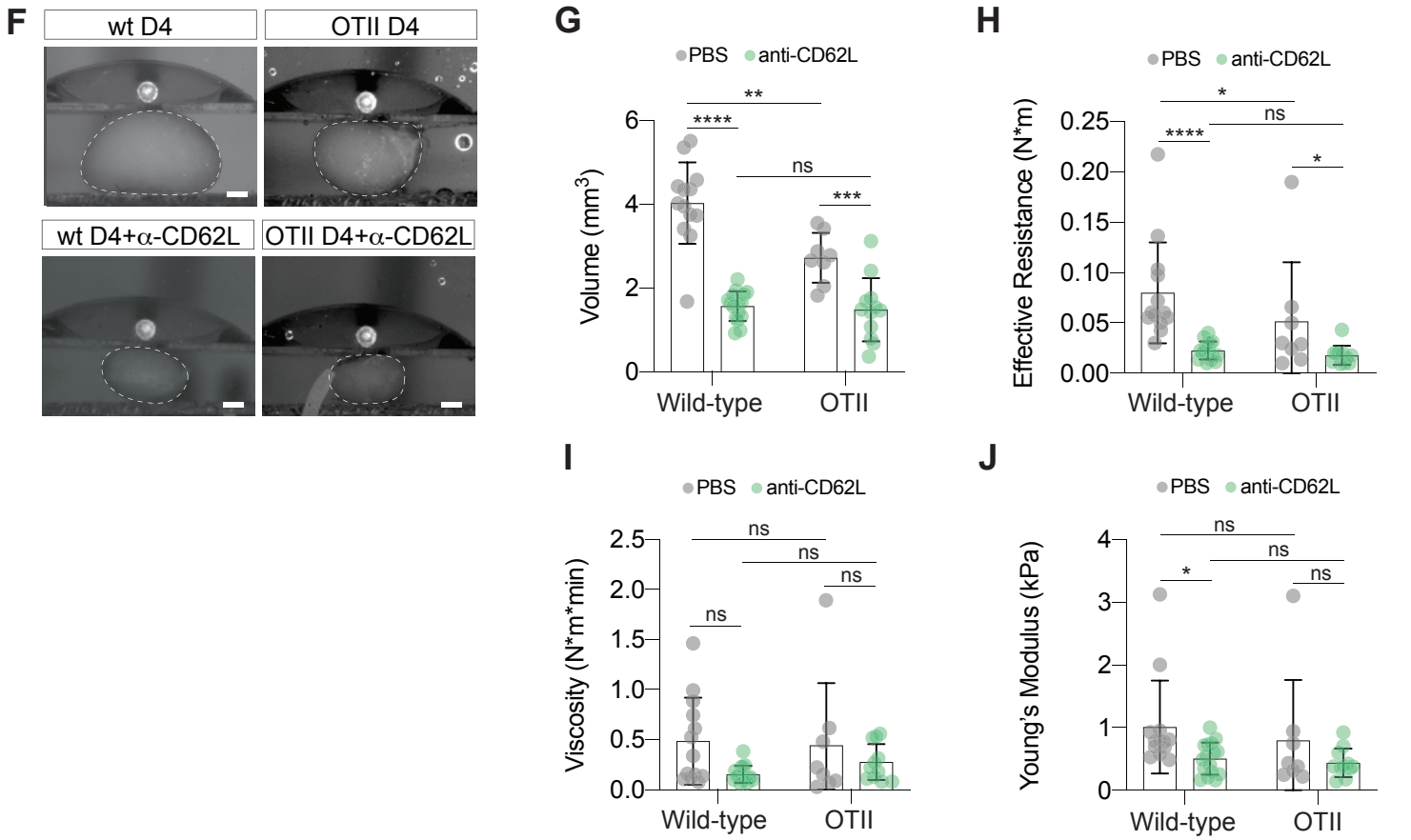

Figure 3

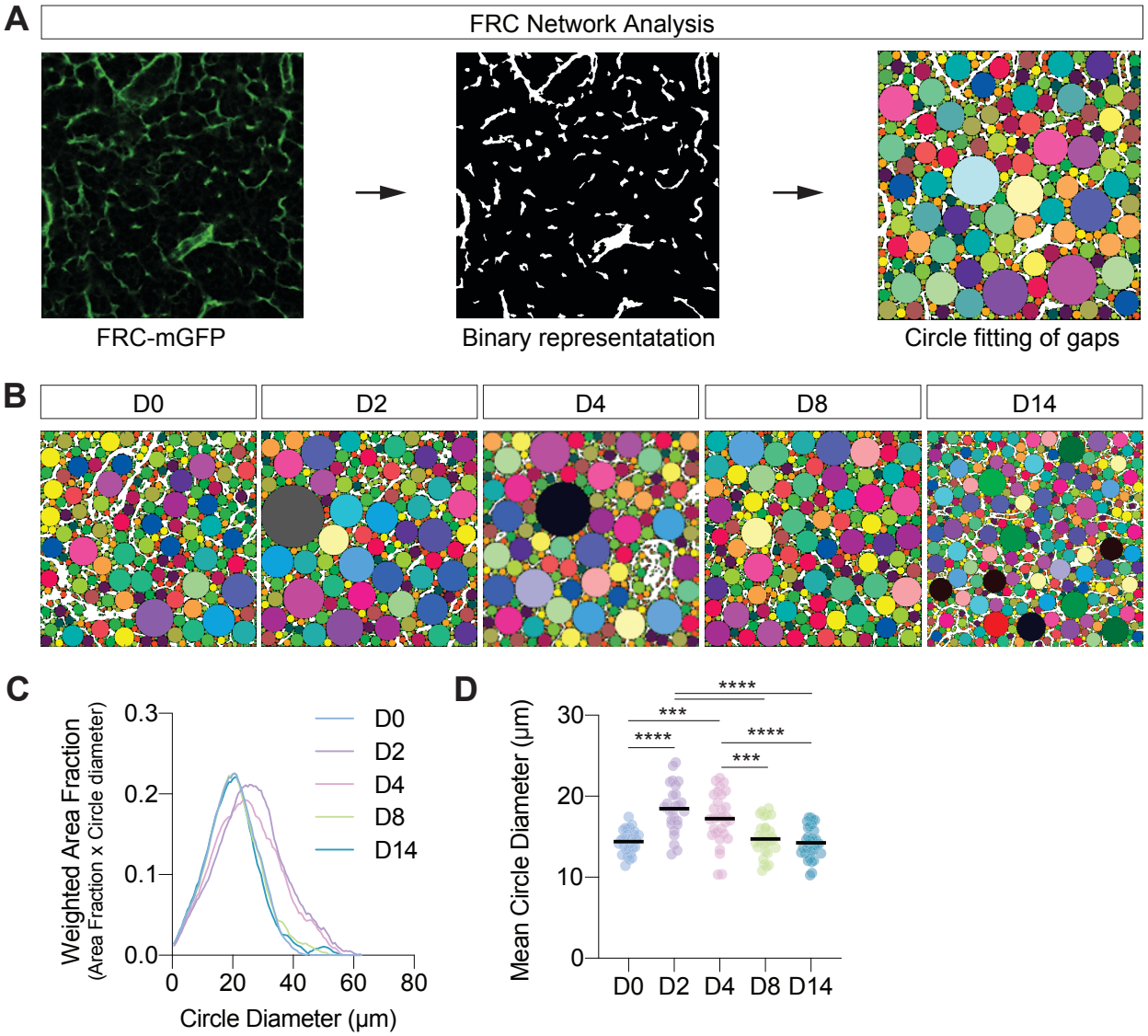
A
FRC Network Analysis
FRC-mGFP
Binary representatation
Circle fitting of gaps
B
D0
D2
D4
D8
D14
C
Weighted Area Fraction
(Area Fraction x Circle diameter)
0.3
0.2
0.1
0.0
0
20
40
60
80
Circle Diameter (µm)
D0
D2
D4
D8
D14
D
Mean Circle Diameter (µm)
30
20
10
0
****
***
****
****
***
D0
D2
D4
D8
D14

Figure 4

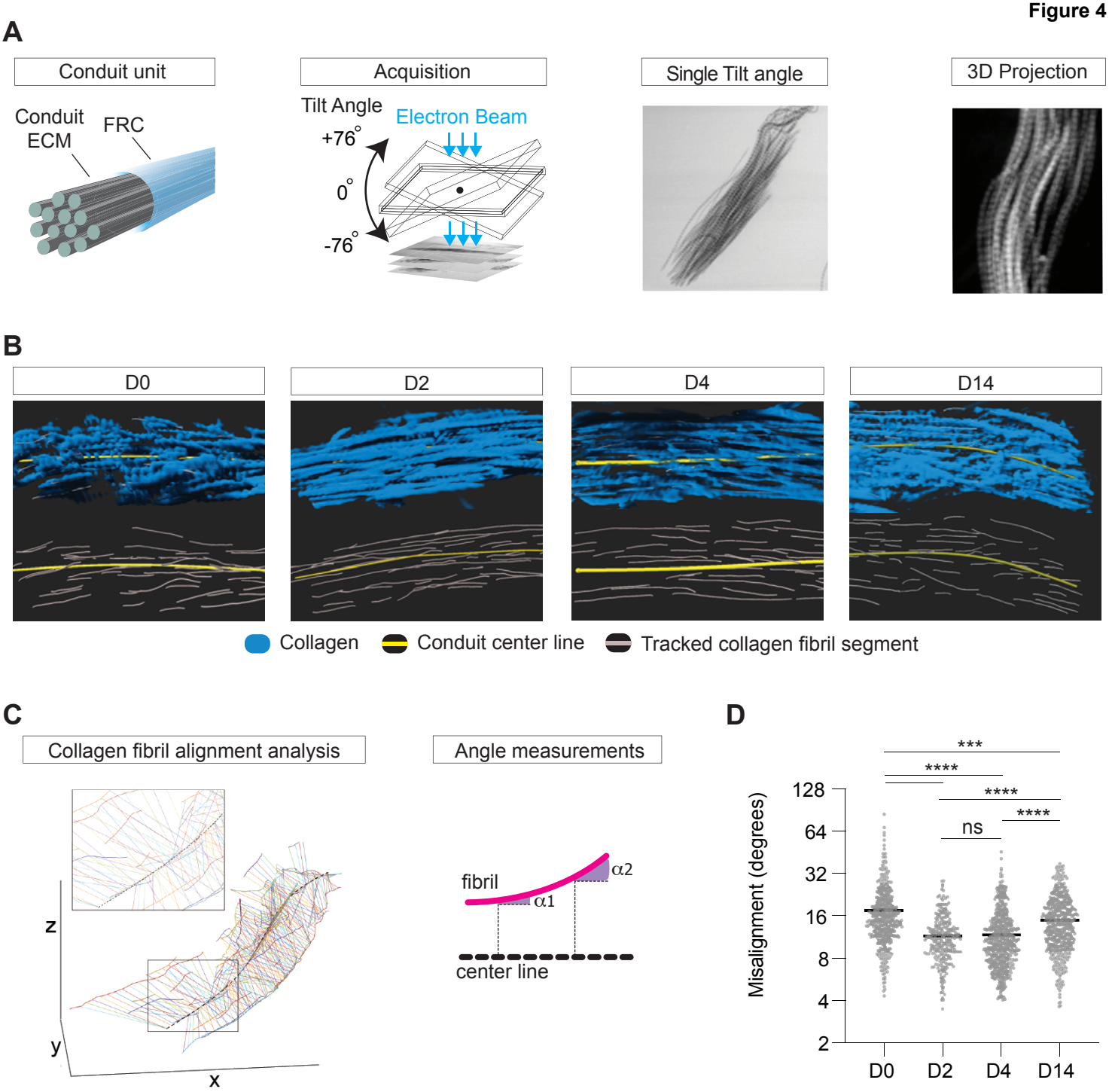
A
Conduit unit
Conduit ECM
FRC
Acquisition
Tilt Angle
Electron Beam
+76°
0°
-76°
Single Tilt angle
3D Projection
B
D0
D2
D4
D14
Collagen
Conduit center line
Tracked collagen fibril segment
C
Collagen fibril alignment analysis
Angle measurements
z
y
x
fibril
α1
α2
center line
D
Misalignment (degrees)
128
64
32
16
8
4
2
***
****
****
ns
****
D0
D2
D4
D14

Figure 5

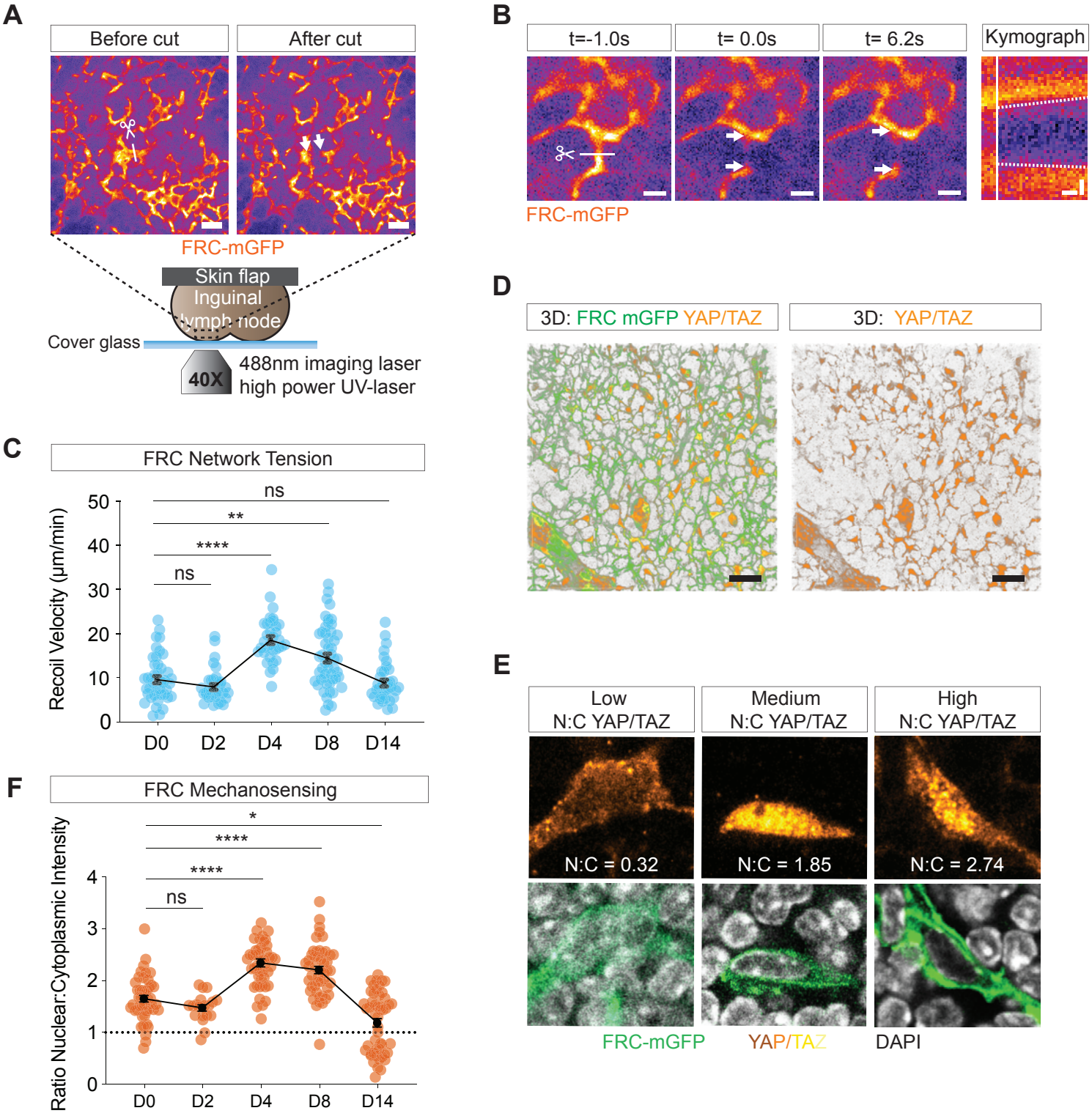
A
Before cut
After cut
FRC-mGFP
Skin flap
Inguinal lymph node
Cover glass
40X
488nm imaging laser
high power UV-laser
B
t=-1.0s
t= 0.0s
t= 6.2s
Kymograph
FRC-mGFP
C
FRC Network Tension
Recoil Velocity (µm/min)
ns
**
****
ns
D0
D2
D4
D8
D14
D
3D: FRC mGFP YAP/TAZ
3D: YAP/TAZ
E
Low N:C YAP/TAZ
Medium N:C YAP/TAZ
High N:C YAP/TAZ
N:C = 0.32
N:C = 1.85
N:C = 2.74
FRC-mGFP
YAP/TAZ
DAPI
F
FRC Mechanosensing
Ratio Nuclear:Cytoplasmic Intensity
*
****
****
ns
D0
D2
D4
D8
D14

Figure 6

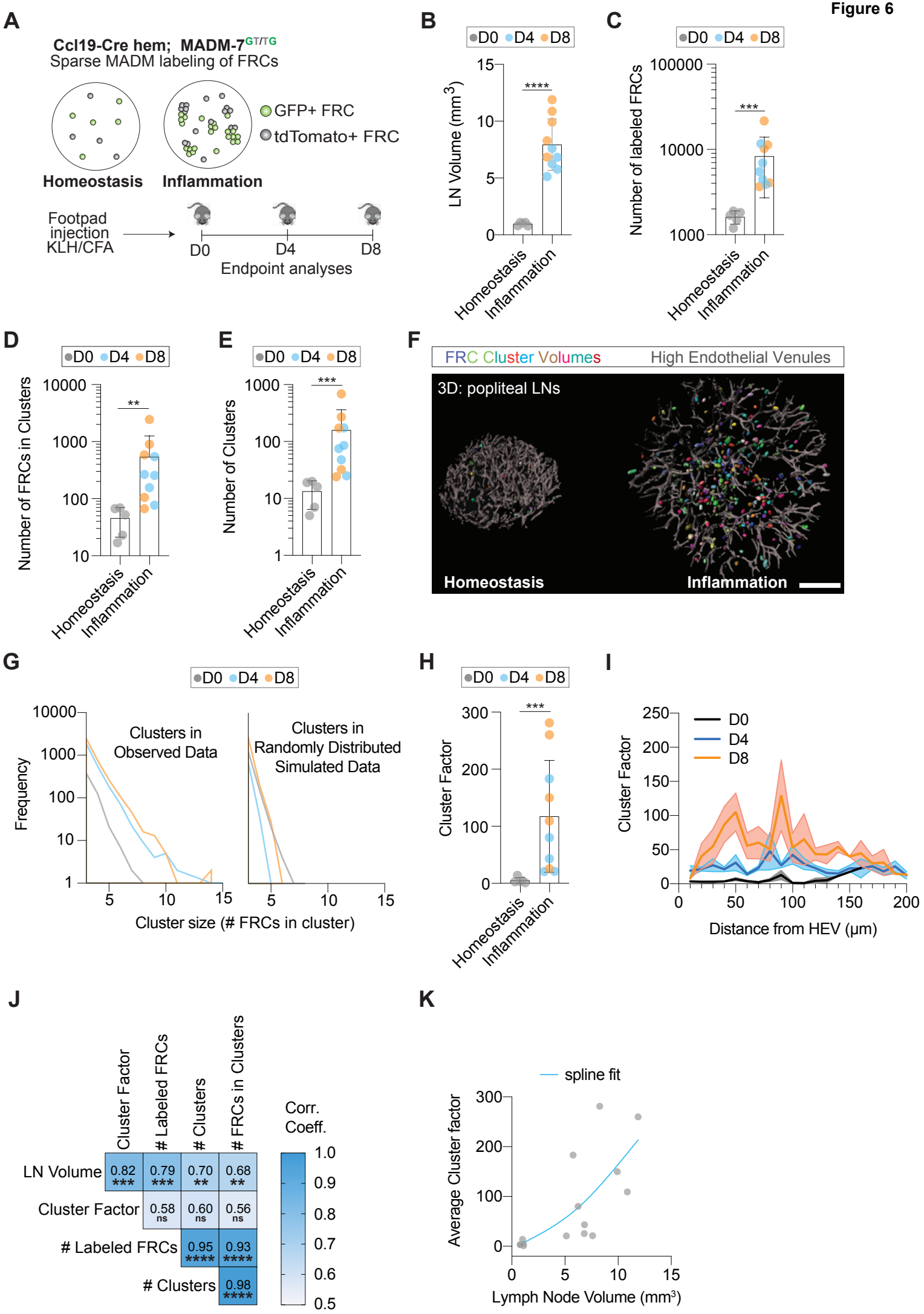
A
Ccl19-Cre hem; MADM-7GT/TG
Sparse MADM labeling of FRCs
GFP+ FRC
tdTomato+ FRC
Homeostasis
Inflammation
Footpad injection KLH/CFA
D0
D4
D8
Endpoint analyses
B
D0 D4 D8
LN Volume (mm3)
****
Homeostasis
Inflammation
C
D0 D4 D8
Number of labeled FRCs
***
Homeostasis
Inflammation
D
D0 D4 D8
Number of FRCs in Clusters
**
Homeostasis
Inflammation
E
D0 D4 D8
Number of Clusters
***
Homeostasis
Inflammation
F
FRC Cluster Volumes
High Endothelial Venules
3D: popliteal LNs
Homeostasis
Inflammation
G
D0 D4 D8
Frequency
Clusters in Observed Data
Clusters in Randomly Distributed Simulated Data
Cluster size (# FRCs in cluster)
H
D0 D4 D8
Cluster Factor
***
Homeostasis
Inflammation
I
D0
D4
D8
Cluster Factor
Distance from HEV (µm)
J
Cluster Factor
Labeled FRCs
Clusters
FRCs in Clusters
Corr. Coeff.
LN Volume 0.82 *** 0.79 *** 0.70 ** 0.68 **
Cluster Factor 0.58 ns 0.60 ns 0.56 ns
Labeled FRCs 0.95 **** 0.93 ****
Clusters 0.98 ****
K
spline fit
Average Cluster factor
Lymph Node Volume (mm3)

Figure 7

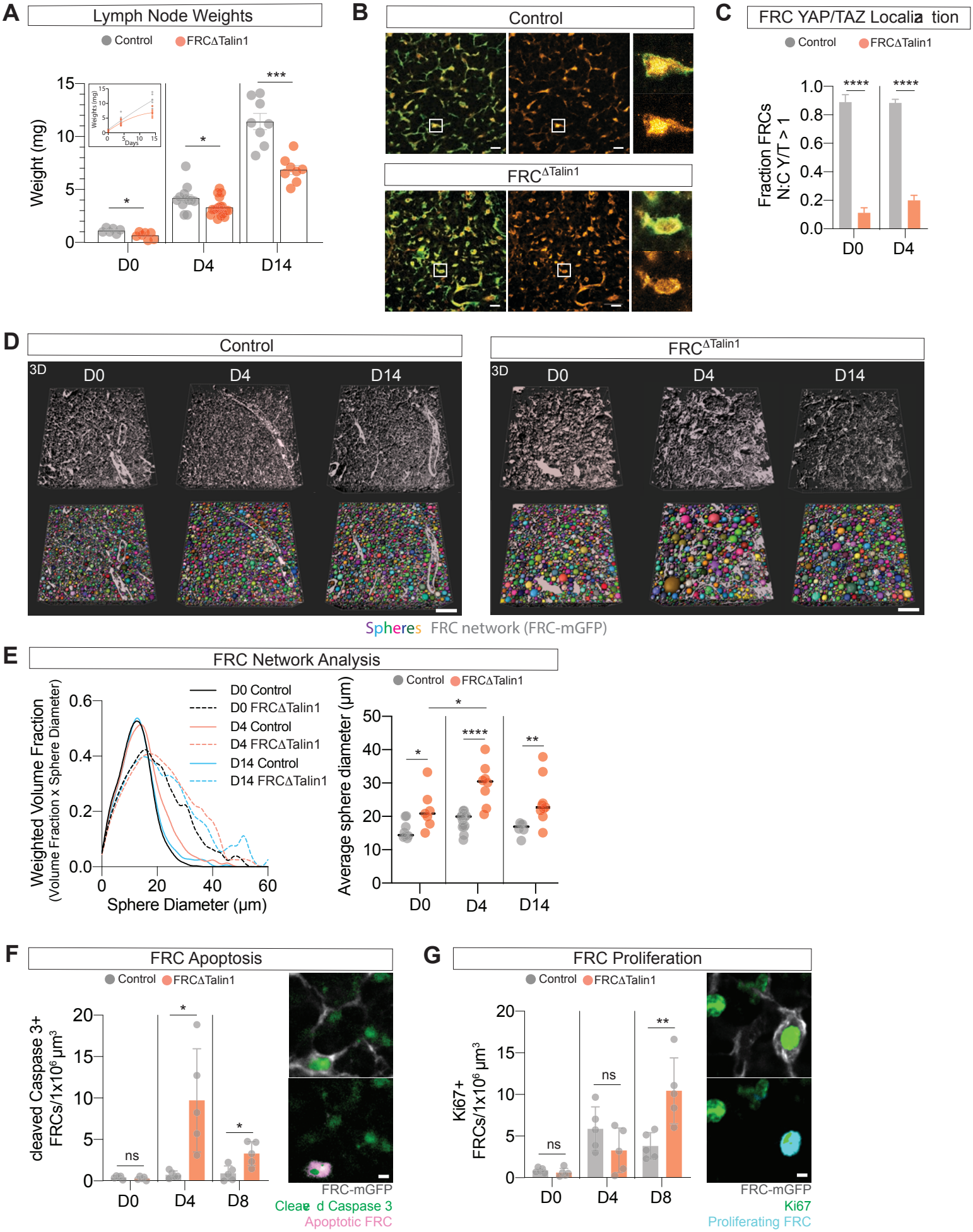
A
Lymph Node Weights
Control
FRCΔTalin1
Weight (mg)
D0
D4
D14
B
Control
FRCΔTalin1
C
FRC YAP/TAZ Localization
Control
FRCΔTalin1
Fraction FRCs N:C Y/T > 1
D0
D4
D
Control
FRCΔTalin1
3D
D0
D4
D14
Spheres
FRC network (FRC-mGFP)
E
FRC Network Analysis
D0 Control
D0 FRCΔTalin1
D4 Control
D4 FRCΔTalin1
D14 Control
D14 FRCΔTalin1
Weighted Volume Fraction
(Volume Fraction x Sphere Diameter)
Sphere Diameter (µm)
Control
FRCΔTalin1
Average sphere diameter (µm)
D0
D4
D14
F
FRC Apoptosis
Control
FRCΔTalin1
cleaved Caspase 3+ FRCs/1x10⁶ µm³
D0
D4
D8
FRC-mGFP
Cleaved Caspase 3
Apoptotic FRC
G
FRC Proliferation
Control
FRCΔTalin1
Ki67+ FRCs/1x10⁶ µm³
D0
D4
D8
FRC-mGFP
Ki67
Proliferating FRC

Figure 8

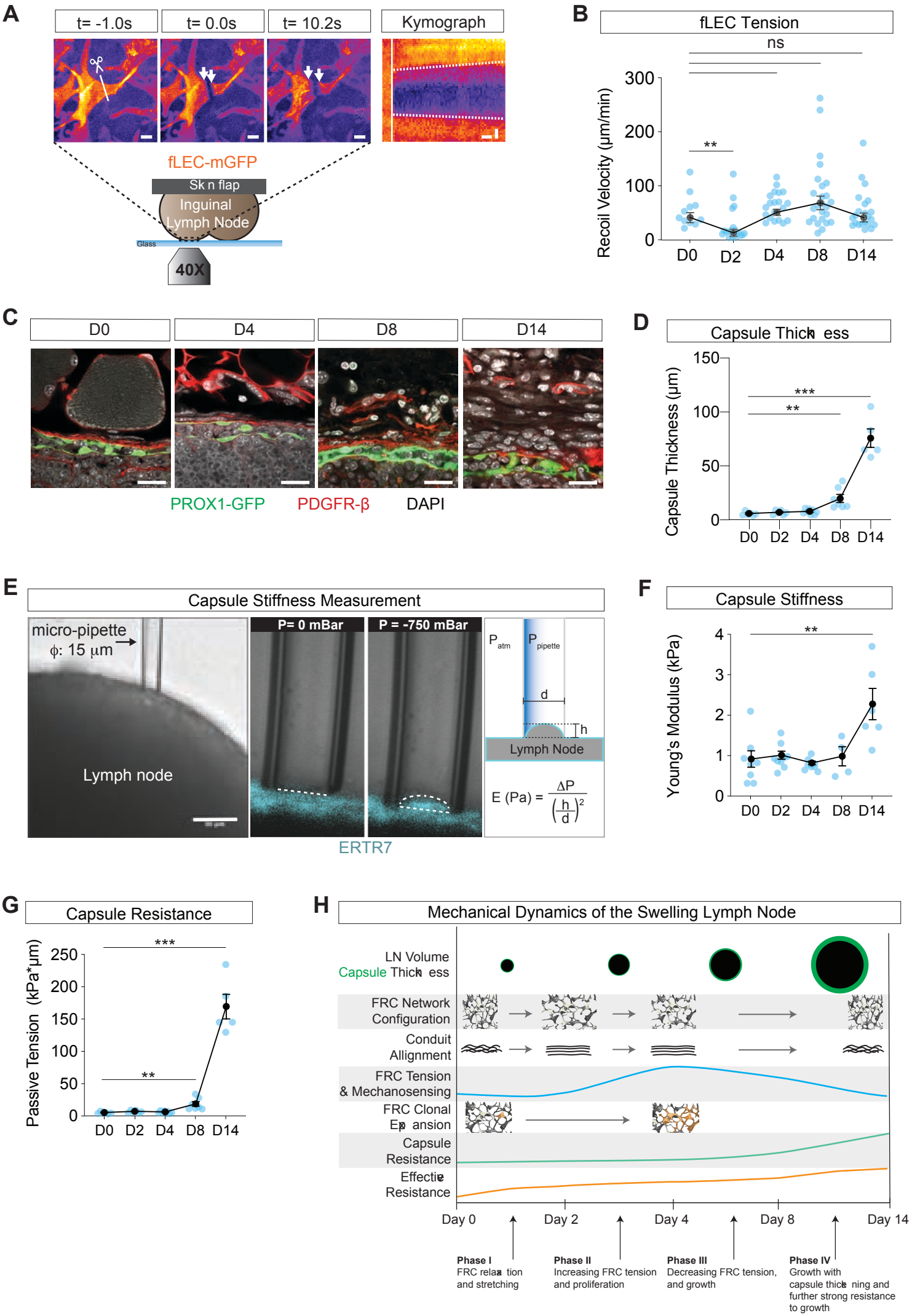
A
t= -1.0s
t= 0.0s
t= 10.2s
Kymograph
fLEC-mGFP
Skin flap
Inguinal Lymph Node
Glass
40X
B
fLEC Tension
ns
**
Recoil Velocity (µm/min)
300
200
100
0
D0
D2
D4
D8
D14
C
D0
D4
D8
D14
PROX1-GFP
PDGFR-β
DAPI
D
Capsule Thickness
***
**
Capsule Thickness (µm)
150
100
50
0
D0
D2
D4
D8
D14
E
Capsule Stiffness Measurement
micro-pipette
ϕ: 15 µm
Lymph node
P= 0 mBar
P = -750 mBar
ERTR7
P atm
P pipette
d
h
Lymph Node
E (Pa) = ΔP / (h/d)²
F
Capsule Stiffness
**
Young's Modulus (kPa)
4
3
2
1
0
D0
D2
D4
D8
D14
G
Capsule Resistance
***
**
Passive Tension (kPa*µm)
250
200
150
100
50
0
D0
D2
D4
D8
D14
H
Mechanical Dynamics of the Swelling Lymph Node
LN Volume
Capsule Thickness
FRC Network Configuration
Conduit Allignment
FRC Tension & Mechanosensing
FRC Clonal Expansion
Capsule Resistance
Effective Resistance
Day 0
Day 2
Day 4
Day 8
Day 14
Phase I
FRC relaxation and stretching
Phase II
Increasing FRC tension and proliferation
Phase III
Decreasing FRC tension, and growth
Phase IV
Growth with capsule thickening and further strong resistance to growth

Supplementary Figure 1

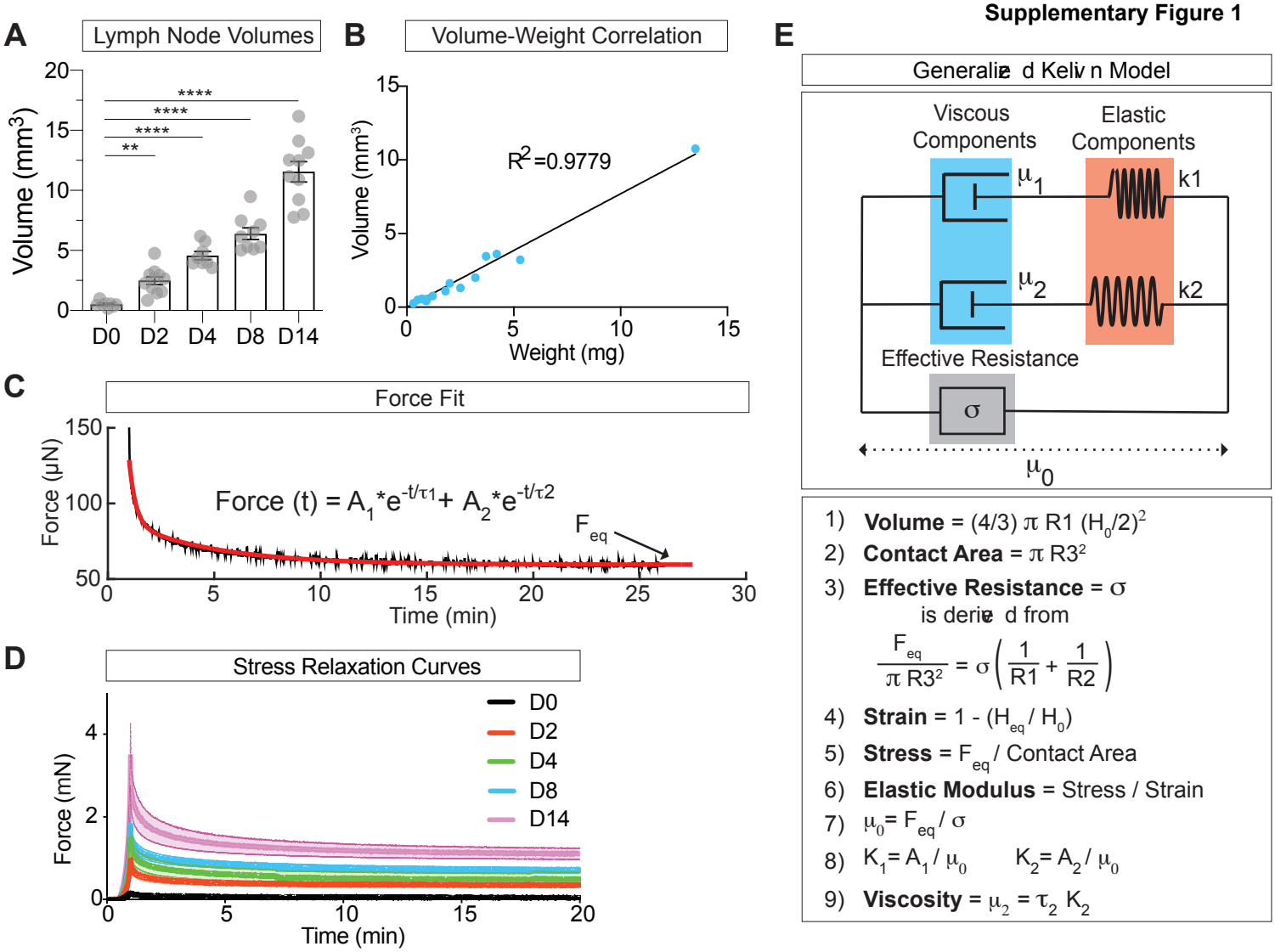

1) **Volume** = $(4/3)\,\pi\, R1\,(H_0/2)^2$
2) **Contact Area** = $\pi\, R3^2$
3) **Effective Resistance** = σ is derived from

$$\frac{F_{eq}}{\pi\, R3^2} = \sigma\left(\frac{1}{R1} + \frac{1}{R2}\right)$$

4) **Strain** = $1 - (H_{eq} / H_0)$
5) **Stress** = F_{eq} / Contact Area
6) **Elastic Modulus** = Stress / Strain
7) $\mu_0 = F_{eq} / \sigma$
8) $K_1 = A_1 / \mu_0$ $\quad K_2 = A_2 / \mu_0$
9) **Viscosity** = $\mu_2 = \tau_2\, K_2$

F

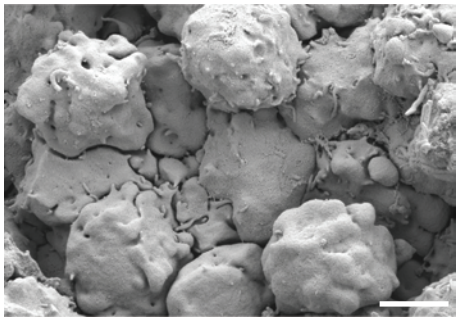

Supplementary Figure 2

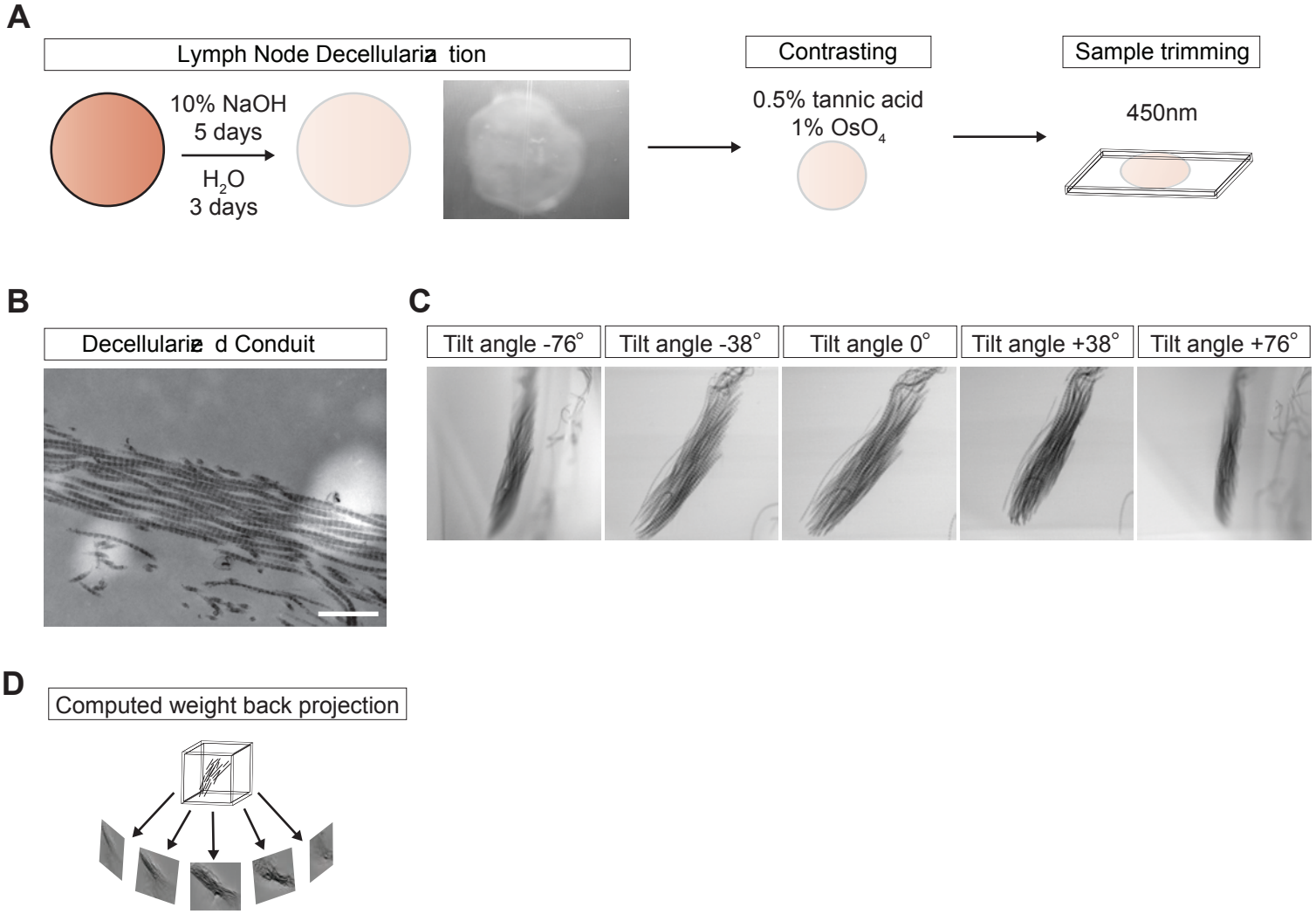

Supplementary Figure 3

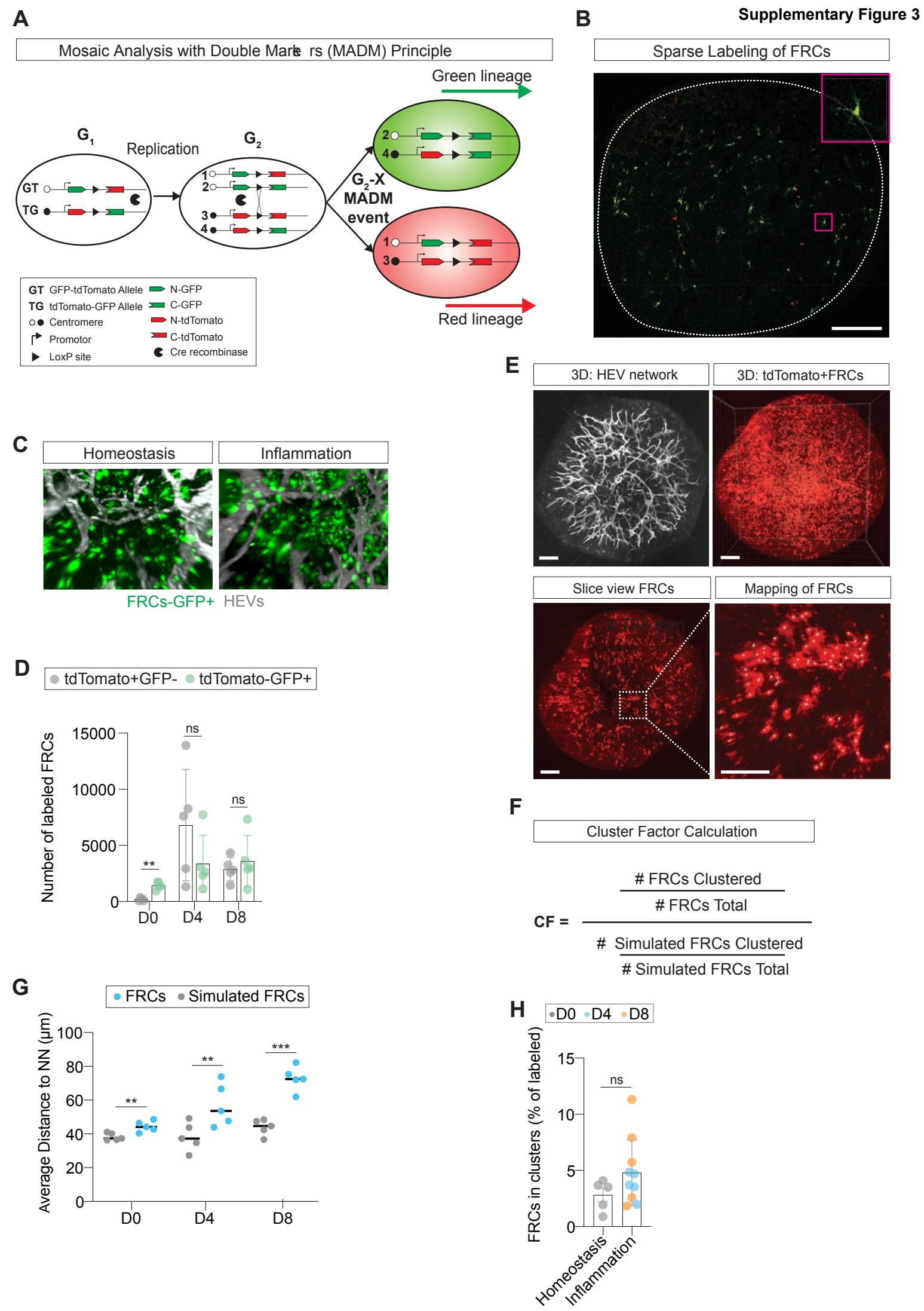

Supplementary Figure 4

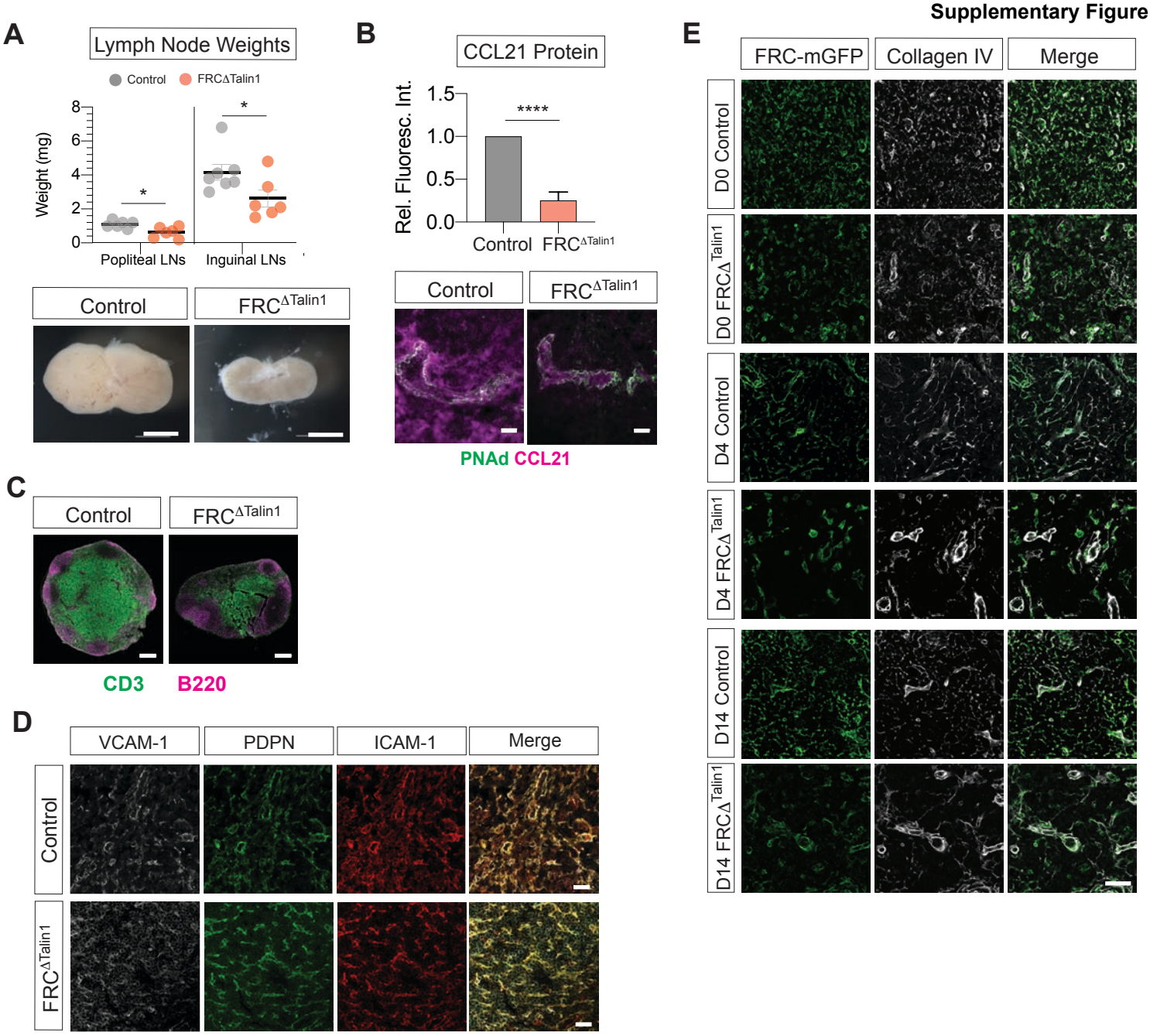

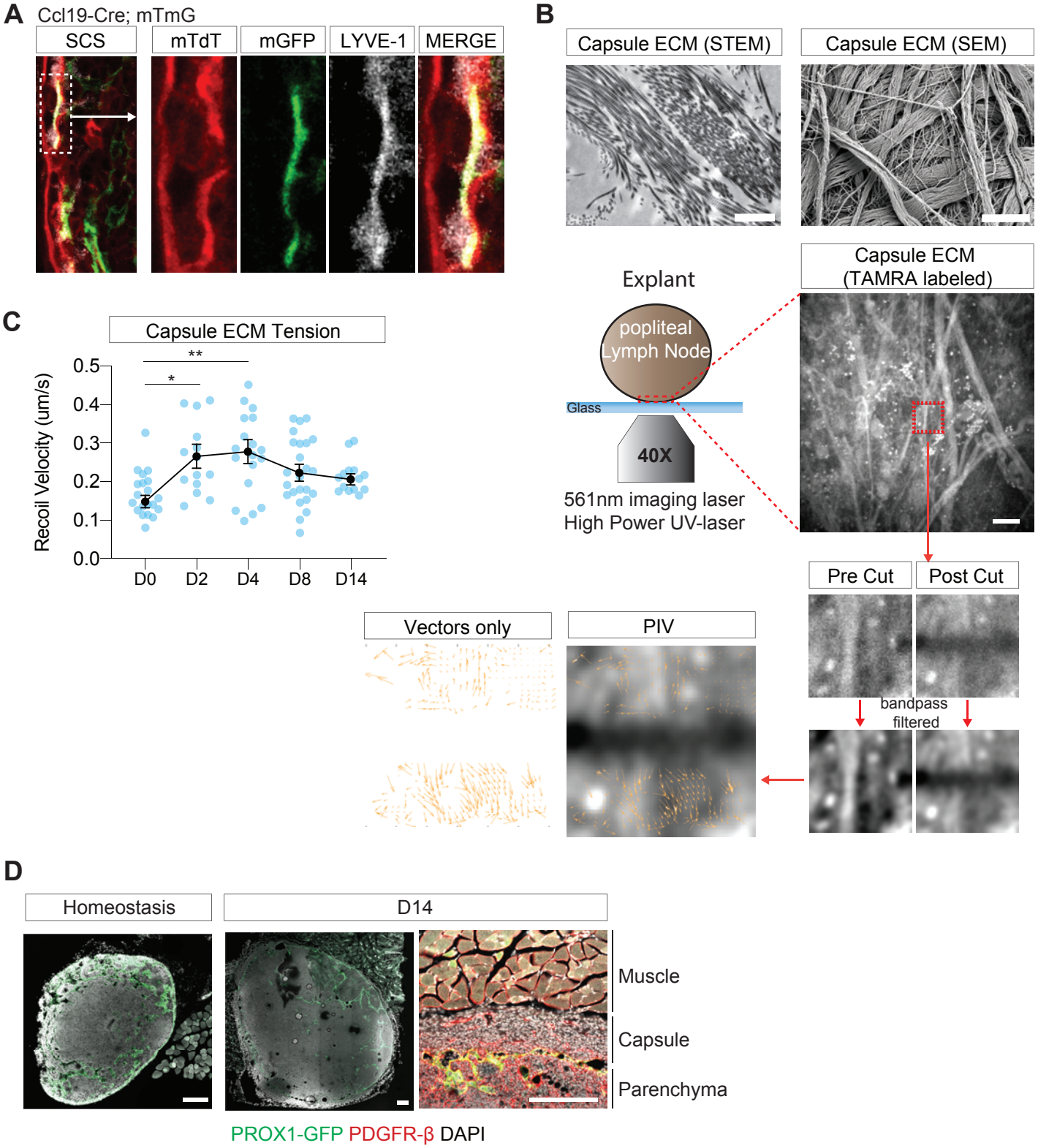
A
Ccl19-Cre; mTmG
SCS
mTdT
mGFP
LYVE-1
MERGE
B
Capsule ECM (STEM)
Capsule ECM (SEM)
Explant
popliteal Lymph Node
Glass
40X
561nm imaging laser
High Power UV-laser
Capsule ECM (TAMRA labeled)
Pre Cut
Post Cut
bandpass filtered
Vectors only
PIV
C
Capsule ECM Tension
Recoil Velocity (um/s)
0.5
0.4
0.3
0.2
0.1
0.0
**
*
D0
D2
D4
D8
D14
D
Homeostasis
D14
Muscle
Capsule
Parenchyma
PROX1-GFP PDGFR-β DAPI